Seasonal variation of the quasi 5 day planetary wave: Causes and consequences for polar mesospheric cloud variability in 2007

K. Nielsen,[1] D. E. Siskind,[2] S. D. Eckermann,[2] K. W. Hoppel,[3] L. Coy,[2] J. P. McCormack,[2] S. Benze,[4,5] C. E. Randall,[4,5] and M. E. Hervig[6]

[1]   We have investigated the 5 day wave in both temperature and water vapor in the stratosphere and mesosphere as seen in the Navy Operational Global Atmospheric Prediction System–Advanced Level Physics High Altitude (NOGAPS-ALPHA) analysis fields for summer 2007. We have compared these fields and the derived saturation ratios with polar mesospheric cloud (PMC) measurements from the AIM satellite. We find that the 5 day wave is variable in both time and space, with significant amplitudes in the temperature wave in August (up to ~6 K). By contrast, the 5 day wave–induced water vapor anomalies remain at a near-constant level throughout the season. During August, the 5 day wave in the NOGAPS-ALPHA saturation ratio and in the occurrence of clouds in the AIM data shows a clear anticorrelation with bright PMCs forming in the trough of the temperature wave. The analysis shows that the August enhancement in the 5 day wave amplitude acts to extend the PMC season past the time when zonal mean temperatures are saturated with respect to ice. The increased wave amplitude in August is attributed to in situ wave generation and amplification due to baroclinic instability of mean winds at around 0.1–0.01 hPa. The late-season extension of cloud occurrence due to the 5 day wave may explain previous ground-based reports of bright noctilucent cloud displays in August.

Citation: Nielsen, K., D. E. Siskind, S. D. Eckermann, K. W. Hoppel, L. Coy, J. P. McCormack, S. Benze, C. E. Randall, and M. E. Hervig (2010), Seasonal variation of the quasi 5 day planetary wave: Causes and consequences for polar mesospheric cloud variability in 2007, *J. Geophys. Res.*, *115*, D18111, doi:10.1029/2009JD012676.

1.   Introduction

[2]   Planetary Rossby waves with typical periods ranging from ~2–20 days can be categorized either as forced waves, generated by orographic forcing, strong tropical convection, or longitudinal variations in heating [e.g., *Salby*, 1984; *Holton*, 1992], or as free modes, which are resonant responses to atmospheric disturbances. Rossby waves are embedded in Laplace's tidal equation, with the gravest mode being the westward propagating 5 day wave of zonal wave number 1 [*Forbes*, 1995]. The fundamental theory of planetary waves is well developed [e.g., *Ahlquist*, 1982; *Salby*, 1984; *Andrews et al.*, 1987; *Volland*, 1988; *Holton*, 1992; *Forbes*, 1995] and observations have confirmed the basic properties. However,

observations also show significant dynamical variability that is only partially understood.

[3]   The 5 day wave is well documented in the lower atmosphere with strong signatures in pressure and geopotential height [e.g., *Madden and Julian*, 1972; *Madden*, 1978; *Ahlquist*, 1982; *Speth and Madden*, 1983; *Lejenäs and Madden*, 1992]. In the mesosphere it has traditionally been observed in winds measured by ground-based radar systems [e.g., *Lieberman et al.*, 2003; *Riggin et al.*, 2006] or in temperatures measured from satellites [e.g., *Hirooka*, 2000; *Garcia et al.*, 2005]. *Rosenlof and Thomas* [1990] utilized ozone measurements from the Solar Mesosphere Explorer satellite to establish the presence of the 5 day wave in the lower mesosphere, and most recently, *Sonnemann et al.* [2008] reported a quasi 5 day signal in lower-mesospheric water vapor mixing ratios. Other planetary wave modes with periods of around 2, 10, and 16 days are also often observed in the mesosphere [e.g., *Palo and Avery*, 1996; *Azeem et al.*, 2001; *Lawrence and Jarvis*, 2003; *Pancheva and Mitchell*, 2004; *Turnbridge and Mitchell*, 2009].

[4]   In the polar summer mesosphere, planetary waves can potentially modulate high-altitude clouds, commonly referred to as noctilucent clouds (NLCs) by ground-based observers, and as polar mesospheric clouds (PMCs) when observed from space. While ground-based observations have revealed planetary wave modulation of PMCs with periods of 5 and

[1]Computational Physics Inc., Boulder, Colorado, USA.
[2]Space Science Division, Naval Research Laboratory, Washington, DC, USA.
[3]Remote Sensing Division, Naval Research Laboratory, Washington, DC, USA.
[4]Laboratory for Atmospheric and Space Physics, University of Colorado, Boulder, Colorado, USA.
[5]Also at Department of Atmospheric and Oceanic Sciences, University of Colorado, Boulder, Colorado, USA.
[6]GATS Inc., Driggs, Idaho, USA.

Report Documentation Page		*Form Approved* *OMB No. 0704-0188*

1. REPORT DATE **18 FEB 2010**	2. REPORT TYPE	3. DATES COVERED **00-00-2010 to 00-00-2010**

4. TITLE AND SUBTITLE **Seasonal variation of the quasi 5 day planetary wave: Causes and consequences for polar mesospheric cloud variability in 2007**	5a. CONTRACT NUMBER
	5b. GRANT NUMBER
	5c. PROGRAM ELEMENT NUMBER
6. AUTHOR(S)	5d. PROJECT NUMBER
	5e. TASK NUMBER
	5f. WORK UNIT NUMBER
7. PERFORMING ORGANIZATION NAME(S) AND ADDRESS(ES) **Naval Research Laboratory,Space Science Division,4555 Overlook Avenue SW,Washington,DC,20375**	8. PERFORMING ORGANIZATION REPORT NUMBER
9. SPONSORING/MONITORING AGENCY NAME(S) AND ADDRESS(ES)	10. SPONSOR/MONITOR'S ACRONYM(S)
	11. SPONSOR/MONITOR'S REPORT NUMBER(S)

12. DISTRIBUTION/AVAILABILITY STATEMENT
Approved for public release; distribution unlimited

13. SUPPLEMENTARY NOTES

14. ABSTRACT

15. SUBJECT TERMS

16. SECURITY CLASSIFICATION OF:			17. LIMITATION OF ABSTRACT	18. NUMBER OF PAGES	19a. NAME OF RESPONSIBLE PERSON
a. REPORT **unclassified**	b. ABSTRACT **unclassified**	c. THIS PAGE **unclassified**	**Same as Report (SAR)**	**18**	

16 days [*Kirkwood et al.*, 2002; *Kirkwood and Stebel*, 2003], satellite measurements of PMCs have provided us with an opportunity to study the evolution and dynamics of the 5 day wave and its impact on the hemispheric PMC field [*Merkel et al.*, 2003, 2008, 2009; *von Savigny et al.*, 2007]. A westward propagating wave number 2 mode with a period near 2 days has also been documented in the PMC field [*Merkel et al.*, 2008, 2009] which, together with the 5 day wave work of *Kirkwood et al.* [2002] and *von Savigny et al.* [2007], show that planetary wave modulations of PMC properties are strongly coupled to planetary wave temperature oscillations.

[5] The NASA Aeronomy of Ice in the Mesosphere (AIM) satellite is dedicated to the study of PMCs. AIM was launched into a sun synchronous orbit at 600 km altitude on 25 April 2007 with the primary goal of investigating how PMCs form and vary. To attain this goal, AIM carries three instruments: the Solar Occultation For Ice Experiment (SOFIE), which is a solar occultation instrument, the Cloud Imaging and Particle Size (CIPS) experiment, which is a panoramic UV imager, and finally, a dust collector named the Cosmic Dust Experiment (CDE). An overview of the AIM mission and its instruments is provided by *Russell et al.* [2009]. A relatively strong 5 day wave in early August was noted by *Benze et al.* [2009] using PMC occurrence rates from the second generation Solar Backscatter Ultraviolet Instrument (SBUV/2) and CIPS. A more detailed spectral analysis of the CIPS albedo showing 5 day wave–induced cloud variability has been described by *Merkel et al.* [2009] utilizing CIPS imagery from 1 June to 15 August 2007. On comparing these data with Sounding of the Atmosphere using Broadband Emission Radiometry (SABER) temperature measurements, they concluded that most clouds formed within the cold phase of the temperature wave. However, the phase difference between 5 day signals in PMCs and temperature varied between 150° and 180°, supporting earlier inferences by *Merkel et al.* [2008]. *Merkel et al.* [2009] suggested that this varying phase difference could be attributed to the net effects on PMCs of differently phased 5 day wave responses in temperature and water vapor mixing ratios.

[6] In support of the AIM mission, scientists at the Naval Research Laboratory have run their prototype high-altitude global numerical weather prediction (NWP) system, known as the Navy Operational Global Atmospheric Prediction System with Advanced Level and Physics and High Altitude (NOGAPS-ALPHA). This system was used to assimilate satellite measurements of stratospheric and mesospheric temperature, water vapor, and ozone during the first AIM PMC season covering the period 15 May–31 August 2007. These ground-to-mesosphere NOGAPS-ALPHA analysis fields provide a global synoptic view of planetary-scale dynamics that can affect PMC formation. *Hoppel et al.* [2008] described an initial NOGAPS-ALPHA experiment that assimilated high-altitude satellite temperature observations in January 2006 up to 0.01 hPa. *Eckermann et al.* [2009] extended the system to assimilate temperature, water vapor, and ozone observations up to 0.0022 hPa during May–July 2007.

[7] *Eckermann et al.* [2009] studied the planetary wave signals in these analysis fields near the polar summer mesopause using two-dimensional space-time Fourier analysis techniques, revealing the presence of several large-scale waves, with the most prominent being the 5 day wave (westward wave number 1), consistent with the observational findings of *Merkel et al.* [2009]. Other significant wave modes were the migrating diurnal and semidiurnal tides, and a westward propagating wave number 2 mode with a period near 2 days. According to *Eckermann et al.* [2009], the 5 day wave reached its peak amplitude in temperature near the 0.01 hPa level (geometric altitude ~80 km) at 30°N during the month of June. Furthermore, the peak region was extensive, spanning the 20°N–70°N latitude band, with the peak at 70°N occurring at ~77 km altitude. Zonal mean 5 day wave amplitudes showed considerable variability, with major peaks occurring 20 days prior to and after solstice. The largest amplitudes appeared in the 50°N–55°N band. However, significant peak activity was also evident at higher latitudes of 70°N–85°N.

[8] *Eckermann et al.* [2009] also investigated the 5 day wave signal in water vapor mixing ratios and found a peak near 60°N–75°N with amplitudes ~0.2–0.3 ppmv, consistent with ground-based measurements at 69°N by *Sonnemann et al.* [2008]. The subsequent spectral cross-coherence analysis between the wave signals in temperature and water vapor, designed to test the hypothesis of *Merkel et al.* [2009] (that 5 day wave signals in both temperature and humidity control observed 5 day modulation of PMCs), showed no statistically significant correlation at ~5 days. *Eckermann et al.* [2009] attributed this to two possible factors. First, large measurement errors in the assimilated satellite water vapor observations at these altitudes might prevent small 5 day wave–induced water vapor anomalies from being resolved with sufficient accuracy. Second, the reported 5 day wave perturbations in temperature exhibited typical amplitudes, and these moderate wave perturbations may not be sufficiently large to generate responses in the analyzed humidity fields.

[9] *Merkel et al.* [2009] and *Eckermann et al.* [2009] showed that the most dominant planetary wave mode during the 2007 northern hemisphere PMC season was the westward propagating 5 day wave number 1 mode. In this study we investigate its variability, origin, and the phase relations among 5 day wave anomalies in temperature, water vapor, and saturation ratio and observed PMC variability. We utilize the NOGAPS-ALPHA gridded analysis fields covering the full first AIM PMC season from 15 May to 31 August 2007, which extends beyond the periods studied by *Merkel et al.* [2009] and *Eckermann et al.* [2009]. The synoptic fields provide an opportunity to study the 5 day wave in the polar mesosphere in greater temporal and spatial detail utilizing wavelet techniques. As satellite temperature and water vapor observations are assimilated up to 0.0022 hPa, we use the gridded analysis fields and CIPS observations of PMC occurrence frequencies to investigate the phase relations among 5 day wave signals in PMCs, temperature and water vapor at PMC altitudes, to test the hypothesized role of water vapor in affecting PMC brightness modulation by the 5 day wave [*Merkel et al.*, 2009]. Furthermore, we investigate the dynamical impact of the 5 day wave on bright PMCs observed by SOFIE.

[10] Section 2 describes the NOGAPS-ALPHA assimilation system and the specific wavelet techniques applied in this study. Section 3 describes the 5 day wave signatures in NOGAPS-ALPHA temperature, water vapor, and derived

saturation ratio, and how they relate to SOFIE and CIPS cloud observations. Section 4 investigates a significant enhancement in the 5 day wave amplitude during early August and its impact on PMC observations at high latitudes in the late PMC season. Major findings are summarized in section 5.

2. Analysis

2.1. NOGAPS-ALPHA Meteorological Analysis

[11] Here we use 6 hourly global analysis fields at geometric heights $z \sim 0$–90 km generated by an Advanced Level Physics High Altitude (ALPHA) prototype of the Navy Operational Global Atmospheric Prediction System (NOGAPS). *Eckermann et al.* [2009] describe the configuration of the NOGAPS-ALPHA forecast model and data assimilation system used to perform the specific forecast assimilation runs whose analysis output is analyzed here. Briefly, the spectral forecast model was run at T79L68, yielding a quadratic Gaussian grid resolution of $\sim 1.5°$ and vertical resolution in the stratosphere and mesosphere of ~ 2 km extending to 0.0005 hPa. Parameterized nonorographic gravity wave drag was tuned to reproduce observed zonal mean temperature conditions in the mesosphere and lower thermosphere (MLT) during June 2007. In addition to assimilating the usual suite of archived operational sensor data [*Baker et al.*, 2007] (available at http://ams.confex.com/ams/pdfpapers/124031.pdf), the system assimilated version 1.07 temperature retrievals from the SABER instrument on the TIMED satellite and version 2.2 temperature retrievals from the Microwave Limb Sounder (MLS) instrument on the Aura satellite, both over the 32–0.002 hPa range. The system also assimilated version 2.2 MLS water vapor retrievals from 316 to 0.002 hPa and ozone retrievals from 215 to 0.02 hPa. Analysis fields are generated every 6 hours on a regular $1° \times 1°$ grid from the ground to the MLT at a pressure height resolution of ~ 2 km in the middle atmosphere. These isobaric fields can be subsequently regridded to a geometric height grid using analyzed geopotential height fields, following *Stull* [1999]. More details of the assimilation procedures, and initial validation and scientific analysis of the resulting high-altitude analysis products, are given by *Hoppel et al.* [2008] and *Eckermann et al.* [2009].

[12] Since we wish to study these analysis fields at summer MLT altitudes ~ 82–87 km where PMCs are typically observed [*Hervig et al.*, 2009], we focus mostly on analysis fields on output pressure surfaces between about 0.01 and 0.0022 hPa, corresponding roughly to a summer MLT geometric height range of ~ 82–87 km [*Eckermann et al.*, 2009, Figure 11]. Following *Eckermann et al.* [2009], saturation ratios

$$S = \frac{p_{H_2O}}{p_{ice}} \qquad (1)$$

at these MLT pressure levels are computed diagnostically from the NOGAPS-ALPHA temperature and humidity analyses based on the *Murphy and Koop* [2005] parameterization of saturation vapor pressure for ice, as recommended by *Rapp and Thomas* [2004] for PMC studies.

[13] *Eckermann et al.* [2009] profiled these analysis products at summer (northern) MLT altitudes from around 15 May to 15 July 2007. Here we extend that period of

analysis to 31 August. Figure 1 plots time series from 15 May to 31 August of zonal mean temperature, water vapor mixing ratio, and saturation ratios from NOGAPS-ALPHA analysis fields averaged over the PMC altitudes of ~ 82–87 km, within a 10°latitude band centered at 70°N. Progressing forward in time in Figure 1a, the analyzed summer mesopause cools, reaching an average minimum mean temperature of ~ 135 K on 20 June, then warms gradually and irregularly until late August when a sharper warming transition occurs.

[14] Throughout the season there are significant vacillations in these slower zonal mean temperature trends with amplitudes of up to ~ 5 K. It is important to note several practical assimilation issues that can explain a few of the vacillations seen after 15 July. *Eckermann et al.* [2009] did not study analysis products after 15 July, when the TIMED satellite yawed and SABER no longer provided temperature observations at summer polar MLT latitudes for the analysis. The sudden denial of SABER data on this date, marked with the gray line in Figure 1, likely explains the ~ 2 K jump in mean temperatures at this time. The transient ~ 7 K cooling seen on 8 August in Figure 1a is almost certainly an artifact of 2 days of missing MLS data. At these times the system is assimilating no upper stratospheric or MLT observations at all at polar summer MLT latitudes, and thus the analysis fields here are controlled by model forecasts constrained solely by tropospheric and stratospheric initial conditions. Additional forecast model simulations (not shown) indicate that the nonorographic gravity wave drag settings, tuned for June 2007 conditions [see *Eckermann et al.*, 2009, section 3], yield systematic cold "drifts" of summer MLT forecasts by August 2007, consistent with the cooling observed on 8 August in Figure 1a when observations are removed.

[15] Zonal mean water vapor mixing ratios in Figure 1b show a progressive moistening over the season, from ~ 2 ppmv in middle to late May to a maximum of ~ 5.5 ppmv around 25 August. This is in agreement with independent observations [e.g., *Nedoluha et al.*, 1996; *Seele and Hartogh*, 1999], and consistent with a continuous mean upwelling of moister stratospheric air into the summer polar MLT [*Körner and Sonnemann*, 2001]. Transient variability of up to ~ 0.5 ppmv is evident in Figure 1b. Although individual MLS water vapor measurements at these altitudes have large random errors [see *Eckermann et al.*, 2009], the errors in the zonal mean analyzed water vapor should be much smaller, and thus this variability likely reflects geophysical influences of not only wave motions but also of dehydration and sublimation from PMCs in the observations (note that the latter effects are not modeled in the forecasts). Indeed, the broad vertical weighting functions of the MLS water vapor measurement at MLT altitudes probably suppresses the actual amount of analyzed geophysical water vapor variability.

[16] The zonal mean diagnostic saturation ratios in Figure 1c show that summer MLT air becomes supersaturated on or around 1 June, which signals the beginning of the PMC season at these latitudes. As noted by *Eckermann et al.* [2009], these diagnostic saturation ratios are strongly anticorrelated with local temperatures due to the exponential dependence of S on temperature. If we ignore the 8–10 August anomaly, zonal mean saturation ratios approach or fall below unity by late July. Given that microphysical models of PMC formation require highly supersaturated air masses, Figure 1c would seem to suggest that mean meteo-
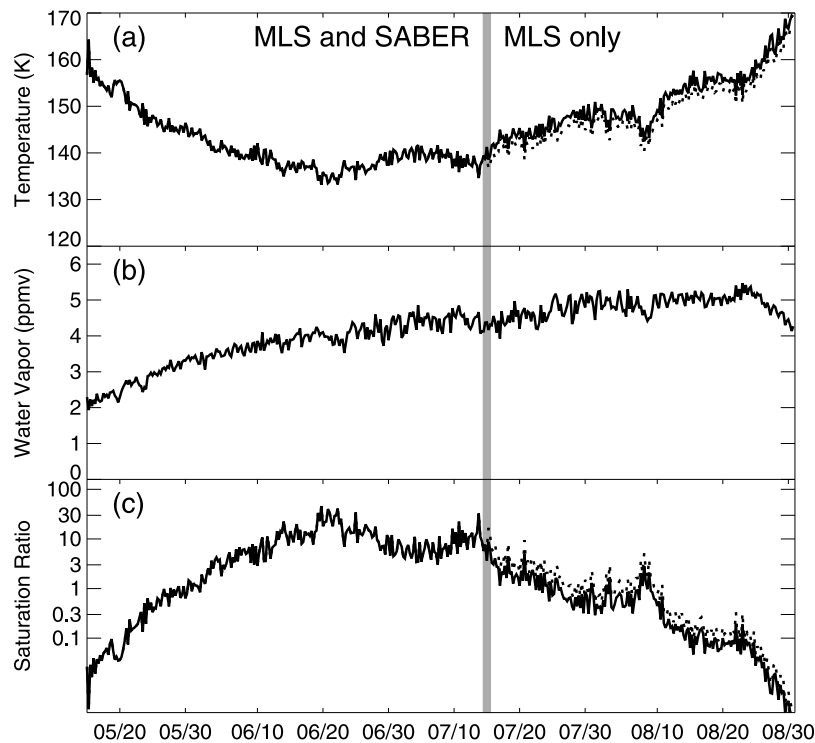
Figure 1. Time series (15 May to 31 August 2007) of (a) zonal mean temperature averaged over the latitude range 65°N–75°N and altitude range 0.006–0.0022 hPa (~82–87 km) and corresponding zonal mean values of (b) water vapor mixing ratio and (c) saturation ratio. A 2 K warm bias due to the absence of Sounding of the Atmosphere using Broadband Emission Radiometry data in the analysis after 14 July (shaded line) is plotted with a dotted curve in Figure 1a, and the corresponding saturation bias is plotted in Figure 1c.

rological conditions should prevent large-scale cloud formation in this latitude band after 25 July, a conclusion that still holds even if possible 2 K warm biases in the temperature analysis after 15 July due to the SABER yaw are factored into the diagnostic S calculations (shown as a dotted line after 15 July in Figures 1a and 1c).

[17] Figure 2 plots the same sequence of temperature, humidity and S fields within the same latitude and time bands as Figure 1, but with the zonal variability now included *via* Hovmöller plots. Temperatures in Figure 2a show two episodes of very cold temperature outbreaks (below 130 K). The coldest period occurs around 18–25 June and covers most longitudes, whereas the secondary cooling on 10–15 July is more localized to the 20°E–180°E longitude band. Another intriguing feature of Figure 2a is a large-amplitude coherent 5 day westward propagating wave 1 disturbance toward the end of the season, beginning around 25 July and persisting throughout August. The water vapor Hovmöller plot (Figure 2b) also exhibits spatial and temporal variability with sporadic evidence of striations throughout the season that resemble the 5 day wave 1 activity seen in temperature. However, the clear 5 day structures observed in the temperature in early August are not as evident in water vapor. Peaks of up to ~8 ppmv occur in relatively small localized regions covering up to ~20° in longitude and lasting less than a day at any given longitude. The variability of ~4 ppmv from 20 to 28 June is much larger than that seen in the zonal averages in Figure 1b, and large moist anomalies intriguingly occur in close proximity (both spatially and temporally) to

the extreme cold regions in Figure 2a. The saturation Hovmöller plot in Figure 2c, which plots only supersaturated ($S > 1$) values, shows that the upper mesosphere between 65°N and 75°N is supersaturated at essentially all longitudes from 1 June to about 20–25 July. Although the zonal mean saturation dropped below unity after 25 July (Figure 1c), the Hovmöller plot clearly shows localized bands of supersaturated air occurring throughout August. The saturation pattern in late July and August in Figure 2c shows the same clear 5 day wave 1 signature seen in temperature (Figure 2a) and suggests PMCs can exist well into August as a result of localized cooling due to a large-amplitude 5 day planetary wave, despite a zonal mean temperature persistently above the frost point at these later times (Figure 1a).

2.2. Instruments

[18] SOFIE measures 16 spectral bands between 0.29 and 5.32 μm with high spatial resolution (~2 km) and sensitivity. The instrument field of view is ~1.5 km (vertical) × 4.3 km (horizontal), while the line of sight covers several hundred km. For a detailed description of SOFIE, see *Gordley et al.* [2009]. One of the science objectives for SOFIE is to determine PMC properties such as particle sizes and ice mass. In this study we use the SOFIE retrievals of ice mass density since this is the fundamental parameter to which the SOFIE 3.064 μm measurements are sensitive [*Gordley et al.*, 2009; *Hervig et al.*, 2009]. During the 2007 NH summer PMC season, SOFIE ice mass densities ranged from 0.1 to 80 ng m^{-3} with an average of 14.2 ng m^{-3}. *Hervig et al.*
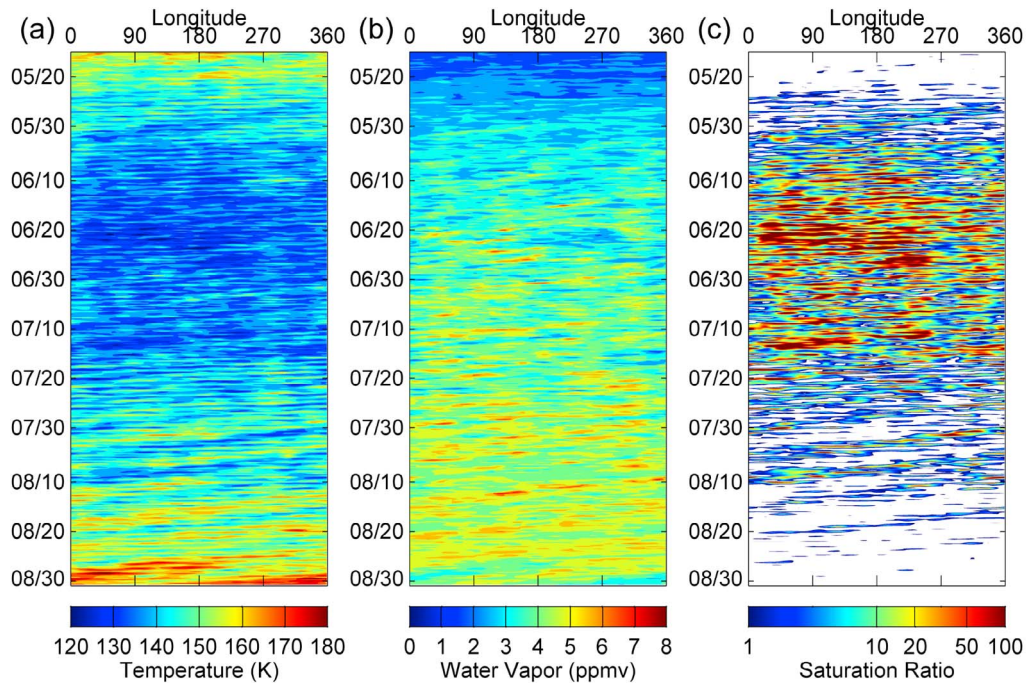
Figure 2. Hovmöller plots of (a) temperature (K), (b) water vapor (ppmv), and (c) saturation as a function of time and longitude. All fields are averaged over a 10° latitude band centered around 70°N and in altitude from 0.006 to 0.0022 hPa.

[2009] provide a detailed explanation of SOFIE observations and the derivation of ice mass density.

[19] CIPS consists of four UV imagers: two nadir-viewing cameras (named MY and PY), one forward viewing camera (PX), and one aft-viewing camera (MX). The four imagers are configured in a cross pattern to create a panoramic image of PMCs with a field of view of 120° × 80° (~2000 × 1000 km). The instrument measures scattered radiation at 265 nm, and identifies PMCs by the enhancements that PMC scattering causes compared to background Rayleigh scattering. The PX camera is most sensitive to PMC detections because it measures mainly forward scattering, which for PMC particle sizes is more intense than backscatter. Throughout this paper we are only considering CIPS data acquired from the PX camera. For a more detailed description of the CIPS instrument see, for example, *Russell et al.* [2009], *McClintock et al.* [2009], and *Rusch et al.* [2009].

[20] The CIPS data used here are based on an algorithm described by *Benze et al.* [2009]. This algorithm was developed in order to compare CIPS nadir data and SBUV/2 results on the same basis. Thus, pixels are averaged into the SBUV-size footprint. This "mega" pixel resembles the SBUV pixel size of 150 × 150 km. The PX analysis takes advantage of forward scattering that can be found in pixels located at the front edge of the PX camera. Thus in the PX analysis, pixels located at the middle of the front edge of the PX camera are averaged into the SBUV-size footprint. An algorithm similar to the SBUV algorithm is used to distinguish cloud points from the Rayleigh background [*Benze et al.*, 2009].

2.3. Wavelet Analysis

[21] The wavelet technique has the advantage, relative to a conventional fast Fourier transform (FFT), of finding both the dominant frequency (wave number) peaks in time (spatial) series as well as their variation and localization as a function of time (position) [see, e.g., *Kaiser*, 1994; *Addison*, 2002]. A wavelet analysis is particularly useful in spectral analysis of data with intermittent or transient signals. In this work we have applied a continuous wavelet transform with complex Morlet basis functions to one-dimensional time series of NOGAPS-ALPHA fields to investigate variability of the 5 day wavefields. The Morlet basis is commonly used to investigate variations in time series as the complex function contains information about both amplitude and phase within the signal [e.g., *Torrence and Compo*, 1998], as outlined in the Appendix. The wavelet analysis throughout this paper is applied to the stationary (detrended) signals.

[22] In the following we investigate the variability of the 5 day wave in the temperature, water vapor, and derived saturation ratios. We explore how these variations may impact PMC variability and how they are related to observed PMC parameters from the SOFIE and CIPS instruments on board AIM. We will also seek an explanation for the observed variability of the 5 day wave in the NOGAPS-ALPHA analysis fields.

3. Results

3.1. Five Day Wave Signature in NOGAPS-ALPHA Analysis Fields

[23] One-dimensional wavelet analysis of the NOGAPS-ALPHA temperature time series in Figure 2 at each longitude point yields the normalized NOGAPS-ALPHA temperature wavelet power spectra averaged over all longitudes in Figure 3. The wavelet power spectrum is normalized by the variance of the original time series, and contour lines for
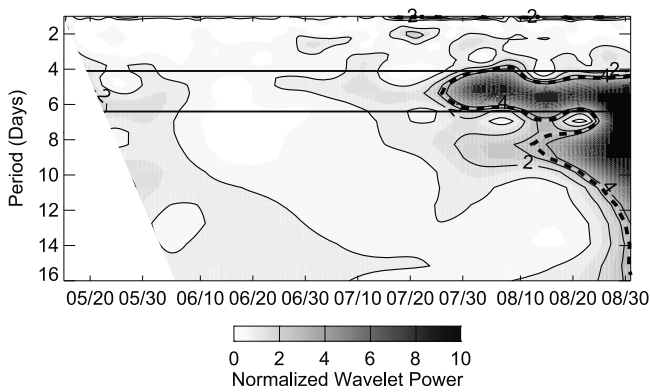
Figure 3. Normalized wavelet power spectrum of the Navy Operational Global Atmospheric Prediction System–Advanced Level Physics High Altitude (NOGAPS-ALPHA) temperature. The wavelet power was calculated for each longitude shown in Figure 2a and then averaged. The contour lines are plotted at normalized wavelet power values of 1, 2, 3, and 4, while the dashed contour line shows the 95% significance level.

normalized wavelet powers of 1, 2, 3, and 4 are also shown. Parts of the spectrum subject to edge effects (cone of influence) are masked as white regions. The dashed black contour shows the 95% significance level. As this work focuses on planetary wave activity, the plot only shows periods up to 16 days.

[24] The most prominent feature of Figure 3 is a burst of 5 day wave activity toward the end of the PMC season, as evident in Figure 2. During the late season there is also evidence of wave activity at periods of 8–10 days. During the main PMC season, the wave power is less for all wave modes as compared to the late-season burst. The westward propagating wave number 2 wave of ~2 day period, discovered by *Merkel et al.* [2009], also shows up in the power spectra within the main PMC season, with amplitudes comparable to those of the 5 day wave during the same time period. On the basis of the mean spectra in Figure 3, we select a bandwidth of 4.1–6.5 days to identify the 5 day wave (bounded by solid black lines). This bandwidth is similar to the one used by *Eckermann et al.* [2009] (4.4–6.2 days) but differs from *Merkel et al.* [2009], who used a bandwidth of 3.8–4.8 days based on spectra obtained from CIPS cloud albedo. Standard two-dimensional space-time Fourier transforms (not shown) applied to the same atmospheric fields revealed a dominant 5 day wave number 1 signal and showed no evidence of other wave numbers associated with a 5 day period [see also *Eckermann et al.*, 2009, Figure 10].

[25] Figure 4 shows a Hovmöller (longitude-time) plot of the resulting wavelet variance in the quasi 5 day band for the temperature (Figure 4a), water vapor (Figure 4b), and saturation (Figure 4c) fields. The altitude and latitude bands are the same as in previous plots (~82–87 km and 65°N–75°N, respectively).

[26] These plots reveal not only large temporal variability, but also significant zonal variations. The temperature variance is relatively low during the main PMC season with typical values <4 K^2 (in fair agreement with the findings of *Merkel et al.* [2009] and *Eckermann et al.* [2009]) with a few sporadic regions of higher variance. A distinct increase in variance around 25 July that spans all longitudes is clearly evident and persists throughout the month of August. Major peaks occur in early August between 90°E and 200°E with wavelet temperature variance of ~25 K^2 as well as at the
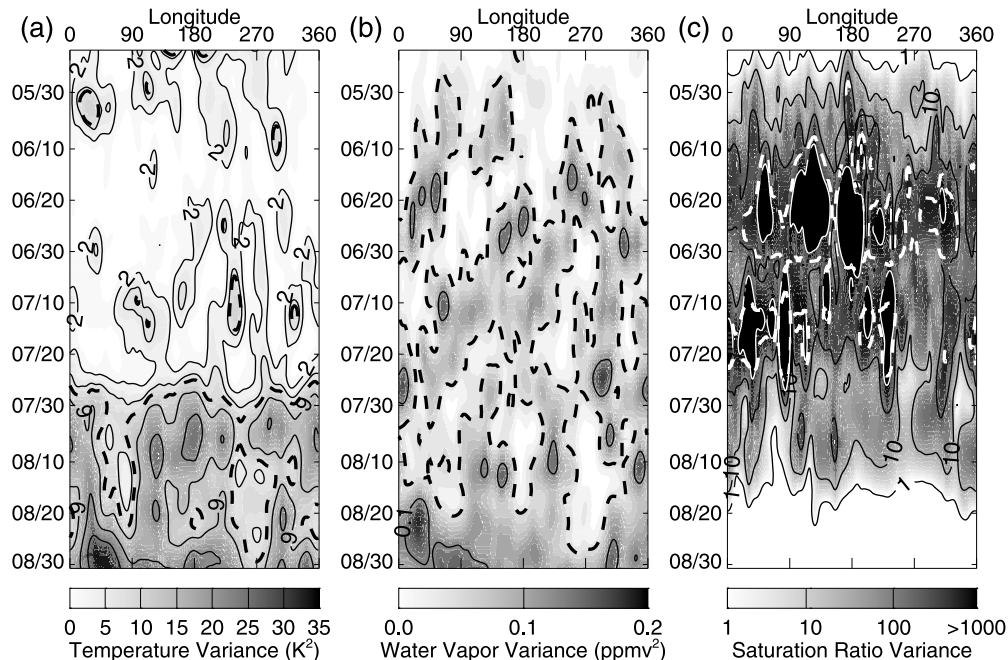

Figure 4. Hovmöller plots of (a) temperature, (b) water vapor, and (c) saturation wavelet variance of the quasi 5 day wave (bandwidth 4.1–6.5 days) evident in Figure 2. In Figure 4a, the contours show 2, 4, 9, 16, and 25 K^2 levels, while the 0.1 ppmv^2 is shown in Figure 4b, and the 1, 10, 100, and 1000 (white) are shown in Figure 4c. The dashed contours show the 95% significance level.
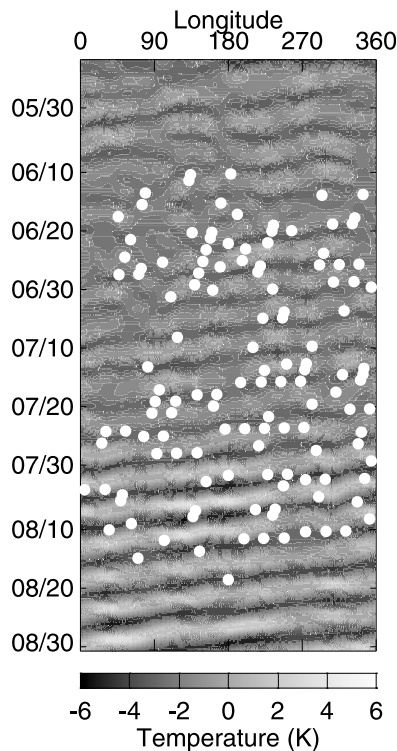
Figure 5. Hovmöller plot of band-passed 5 day temperature oscillations with Solar Occultation For Ice Experiment (SOFIE) bright clouds (indicated by white dots) overplotted. Bright clouds are those of ice mass density >30 ng m^{-3}.

end of August with similar variances. Similar results were obtained by *von Savigny et al.* [2007] during the 2005 northern hemisphere season using MLS temperature data. Their results showed the strongest 5 day signals in early to mid-August. As the end of August is well past the PMC season and air is no longer saturated in the zonal mean sense, we will focus on the early August peaks, which are within time periods where supersaturation does occur.

[27] *Merkel et al.* [2009] analyzed the 5 day wave in SABER temperature data for the period 1 June to 14 July 2007. Their results showed a peak amplitude of ~3 K occurring toward the end of June at 84–88 km and near 77°N. Figure 4a shows the 2 K^2 contour spanning a larger region between 20 and 30 June with peak amplitudes up to ~2 K, in fair agreement with the results of *Merkel et al.* [2009]. More detailed comparisons are complicated by several factors. First, the bandwidth used to identify the 5 day signal is different between the two studies (3.8–4.5 days versus 4.1–6.5 days). Second, our results are averaged over a 10° latitude band and ~7 km altitude range, and are therefore likely to yield a lower mean amplitude as compared to the SABER observations analyzed by *Merkel et al.* [2009]. Third, the amplitude peak observed by *Merkel et al.* [2009] is located outside of our latitude band. However, a similar analysis to *Merkel et al.* [2009] by *Eckermann et al.* [2009] utilizing the NOGAPS-ALPHA analysis temperatures shows similar results.

[28] The water vapor field in Figure 4b shows little seasonal variation in the 5 day wave variance. Occasional peak values in variance of up to ~0.2 ppmv^2 are scattered throughout the

entire PMC season. For comparison, *Sonnemann et al.* [2008] reported amplitudes of ~0.4 ppmv over a period from 15 April to 15 June 2003. Our relatively small values are very similar to the values reported by *Eckermann et al.* [2009] and may be due to a low signal-to-noise ratio in MLS water vapor data and the very broad MLS vertical weighting function at these high altitudes, which may suppress resolved variability. The distinct differences in 5 day wavelet variance between temperature and water vapor may also reflect different driving mechanisms for 5 day wave activity in the temperature and water vapor fields, such as sublimation/ formation of PMCs and advection [*Sonnemann et al.*, 2008].

[29] The saturation variance in Figure 4c is strongest during the mid-PMC season. This is not surprising since the saturation ratio depends exponentially on temperature, and will be most sensitive to small temperature changes during the coldest part of the season. However, it is of great interest to see the strong variances (~100) in early August colocated (in time and space) with the peaks in 5 day temperature variance. This period is characterized by striations of saturation ratio exhibiting peak values up to ~10 within regions where the air is no longer saturated in the zonal mean sense (see Figures 1c and 2c).

[30] Previous results have shown that the 5 day signal in PMCs is highly correlated with the 5 day signal in temperature [*Kirkwood et al.*, 2002; *von Savigny et al.*, 2007; *Merkel et al.*, 2008, 2009]. Our observations support that finding. Furthermore, our results not only show a strong correlation between the 5 day signatures in saturation and temperature, but strongly suggest that favorable conditions for late 2007 season PMC formation are controlled by 5 day wave dynamics. That is, without this surge in 5 day planetary wave activity, late-season PMCs would not exist. Caution is required when interpreting the late-season saturation as it occurs well outside the indicated 95% significance level. Owing to the nonlinear temperature dependence, saturation variance changes throughout the season (peaking during the midseason) and therefore would require a more sophisticated nonstationary significance test as opposed to the stationary test employed here to fully quantify significance levels. However, due to the strong temperature signal and clear correlated signal in saturation, we are confident that these late-season signals are due to the 5 day temperature wave.

[31] Given the significant spatial and temporal variability of the 5 day wave, it is of interest to investigate how the above results relate to observed PMCs. To investigate the impact, we utilize in the following sections PMC observations from the SOFIE and CIPS instruments on board the AIM spacecraft.

3.2. SOFIE

[32] During the 2007 Northern Hemisphere (NH) PMC season SOFIE observed a latitude band ranging from 66°N– 76°N with an average latitude of 68.9°N and began observations on 20 May. SOFIE's unprecedented high sensitivity to PMC ice is evident in that *Hervig et al.* [2009] detected ice in 81% of the occultations during the 2007 NH PMC season, and suggested that ice is present to some extent throughout the polar summer. To investigate the relationship between observed ice mass density and the NOGAPS-ALPHA 5 day planetary wave, Figure 5 plots time series at each longitude of the NOGAPS-ALPHA 5 day
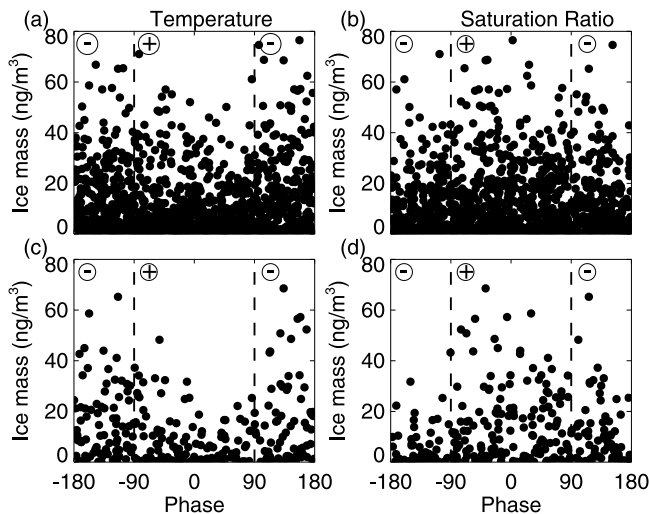
Figure 6. Scatterplots of SOFIE ice mass as a function of (left) the 5 day temperature and (right) saturation wave phase. (a, b) Clouds detected during the entire 2007 Northern Hemisphere season. (c, d) Only clouds detected in August 2007. Negative to positive phase transition implies temperature going from cold to warm.

wave temperature signal from the wavelet analysis at 65°N–75°N. Note that these time series retain phase, and when plotted together in Hovmöller form at their individual longitudes, a 5 day wave signal of zonal wave number 1 becomes clearly evident. SOFIE bright cloud detections are superimposed as white dots. Here we have defined bright clouds as those with ice mass densities >30 ng m^{-3} (the rationale for this choice will become evident in the later discussion accompanying Figure 6). There is an apparent tendency toward bright clouds being situated in the cold trough of the 5 day wave during the entire PMC season, in particular, during the late season after 25 July.

[33] A more quantitative analysis is provided in Figure 6, in which the SOFIE ice mass is plotted as a function of the phase of the 5 day temperature (Figure 6, left) and saturation (Figure 6, right) anomalies. The positive and negative phases are illustrated by circles with plus and minus symbols, respectively. All clouds detected by SOFIE during the course of the PMC season are plotted in Figures 6a and 6b, which show that clouds with ice mass density ≤60 ng m^{-3} display no particular preference for formation in the cold phase of the temperature wave or phase associated with a positive perturbation in saturation ratio. In contrast, 80% of clouds with very high ice mass density (>60 ng m^{-3}) are observed within the cold phase of the wave. In Figures 6c and 6d only clouds detected during the month of August are plotted. The tendency for the higher ice mass density clouds to exist in the negative (positive) temperature (saturation ratio) phase is even clearer during August, with 78% (32) of the clouds with ice mass density >30 ng m^{-3} observed in the cold phase. A similar preference is seen when SOFIE ice is sorted according to the phase of the 5 day signal in NOGAPS-ALPHA saturation ratio (Figure 6, right), where a similar majority of bright clouds are formed in the phase associated with enhanced saturation.

[34] Together with our previous results in section 3.1, Figures 5 and 6 provide additional support for the findings of *von Savigny et al.* [2007] that relatively bright PMCs observed during the late PMC season are formed in the coldest phases of the large-amplitude 5 day wave that is present in the summer polar mesosphere at this time.

3.3. CIPS

[35] PMCs are brighter at higher latitudes, making PMC detection there easier. In our analysis of the CIPS data and subsequent comparison to NOGAPS-ALPHA gridded analysis fields, we have analyzed data within a 10° latitude band centered at 80°N, as compared to the 65°N–75°N band we considered in the SOFIE analysis. Figure 7 is similar to Figure 2 but shows the NOGAPS-ALPHA temperature (Figure 7a), water vapor (Figure 7b), and derived saturation ratio (Figure 7c) fields for the latitude band 75°N–85°N and altitude range 82–87 km. The overall structures are similar at the two latitude bands, with the temperature exhibiting the coldest values from mid-June to mid-July but with the higher latitude band being ~10 K colder. The apparent warming period in early July is also present at these higher latitudes, as well as the obvious presence of a 5 day wave oscillation in early August. In contrast to the lower latitude band shown in Figure 2b, a 5 day wave signature in water vapor mixing ratio is not apparent in these higher-latitude data. The lower amount of water vapor available at the higher latitudes during the main PMC season may reflect a greater degree of dehydration due to freeze-drying by the more prevalent PMCs. As the PMC season nears its end, fewer clouds form and an apparent increase in humidity occurs. This is illustrated in Figure 7c, which shows supersaturated air (S > 1). The saturation ratio decreases significantly after 10 August, which coincides with the apparent jump in water vapor mixing ratios. The plot also shows that saturation ratios are significantly larger in the higher latitude band (compare Figure 2c), illustrating the exponential dependence on temperature and the strong effect even small temperature changes have on the conditions for PMC formation. The late-season wavelet variance and time series (not shown) are similar to the results obtained from the 65°N–75°N latitude band with the exception that the higher latitude band exhibits lower temperature and water vapor variances.

[36] Figure 8a plots the CIPS PMC occurrence frequencies in Hovmöller form. Figure 8b plots the corresponding variance in the 5 day band from a wavelet analysis of these CIPS PMC time series with the 95% significance levels enclosed by the white contour lines. Figure 8c plots the corresponding 5 day time series from a wavelet analysis of the CIPS PMC data, revealing the amplitude and phase of the observed quasi 5 day PMC variations. The latitude range in these Hovmöller plots is 75°N–85°N. The daily occurrence frequency is calculated on a 1°longitude grid. However, since only a small portion of the available CIPS data is used due to the SBUV-size footprint, a 20° running average over longitude has been applied in order to avoid large gaps. The wavelet analysis is applied as in section 3.1 with a bandwidth covering the periods 4.1–6.5 days.

[37] The cloud occurrence frequency in Figure 8a peaks during the main PMC season from approximately 15 June
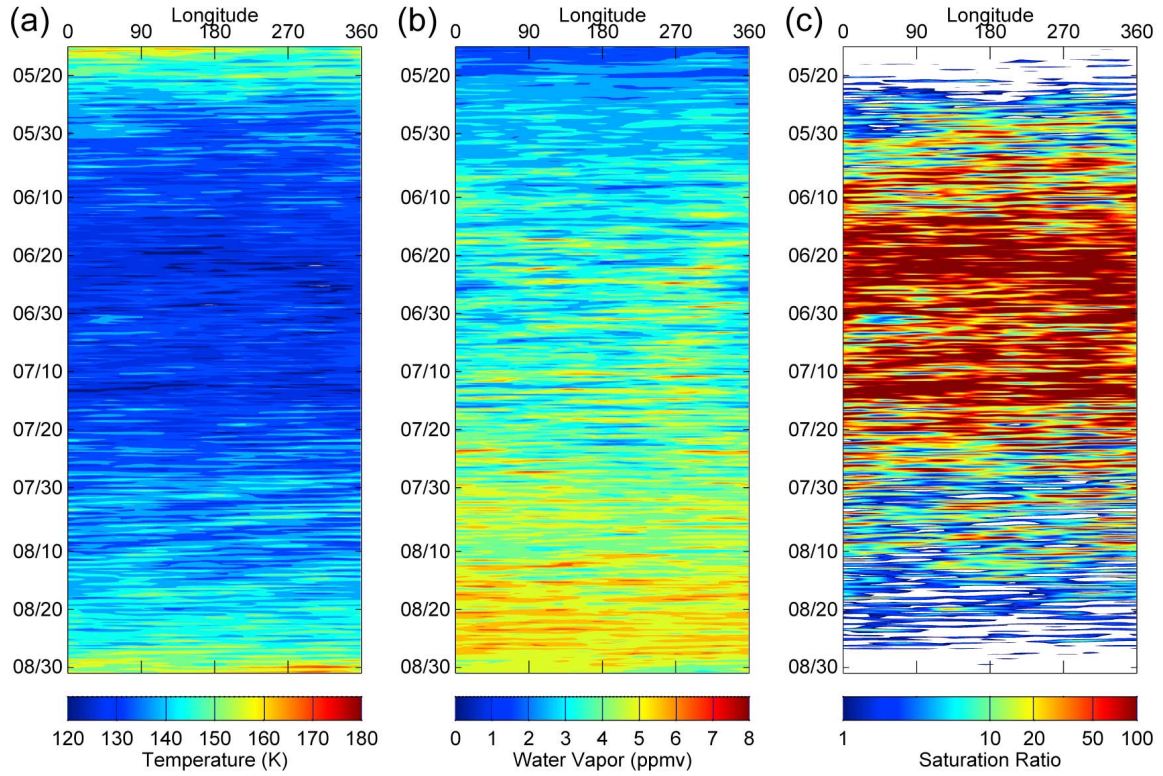
Figure 7. As in Figure 2, but now covering the latitude band of 75°N–85°N.
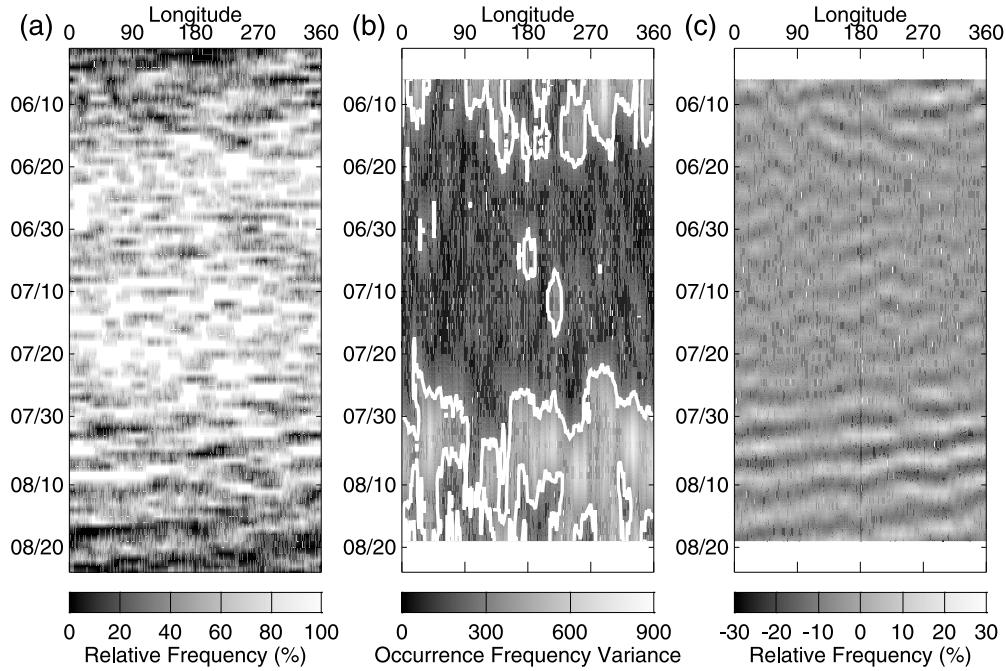

Figure 8. Hovmöller plots of (a) Cloud Imaging and Particle Size (CIPS) cloud occurrence frequency, (b) the filtered 5 day wavelet variance (percentage squared) in CIPS cloud occurrence with the 95% significance level (white contours), and (c) the associated wavelet amplitude. The white areas in Figures 8b and 8c at the beginning and end are regions outside the cone of influence.
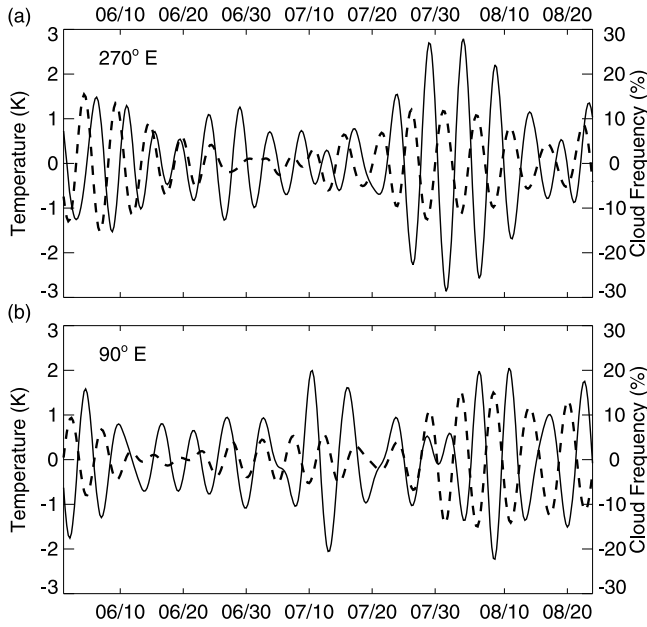
Figure 9. Time series of the band-passed 5 day wave in NOGAPS-ALPHA temperature (solid line) and CIPS cloud frequency (dashed line; taken from Figure 7) at two different longitudes: (a) 270°E and (b) 90°E.

to 25 July, although there is a period of ~10 days from 30 June to 10 July with an apparent drop in cloud frequency. This agrees well with the NOGAPS-ALPHA temperature shown in Figure 7, in which the coldest temperatures are seen during the same period, with a slight warming period in early July lasting roughly 10 days as was also seen in SOFIE PMC data at lower latitudes [*Eckermann et al.*, 2009]. *Merkel et al.* [2009] showed a similar reduction in CIPS cloud albedo coincident with warm SABER temperatures. The CIPS PMC occurrence frequency also exhibits a clear modulation by the 5 day wave in August, which is reminiscent of the signature seen in NOGAPS-ALPHA temperature. The late-season amplitudes (up to 100%) exhibit similar peak values to those seen during the main PMC season. This is in contrast to what would have been observed using cloud albedo, as the albedo becomes less bright as the season progress toward warmer mean temperatures.

[38] The 5 day wavelet variance of CIPS cloud frequency is shown in Figure 8b. The contour values are masked at the initial and end times where edge effects may affect the wavelet transform. During the main PMC season the variance (in units of percentage squared) exhibits typical values of ~100–300 with isolated peak values of ~500 in early June and July. High variance (up to ~900) is present during the early August period, in concert with NOGAPS-ALPHA temperature at the lower latitude band (65°N–75°N) (section 3.1), indicating that the 5 day planetary wave seen in the assimilated temperature (and derived saturation ratio) also appears strongly in the PMC field during the late 2007 PMC season. A similar observation was reported by *von Savigny et al.* [2007] for the 2005 northern hemisphere PMC season. The corresponding time series of amplitude and phase of CIPS PMC occurrence frequency in the 5 day band (Figure 8c)

reveals a relatively strong, coherent phase structure in the late season with amplitudes of up to ~30%. This clear wave structure provides us with an opportunity to investigate the phase relationship between the 5 day wave signal in CIPS and the corresponding 5 day signals in analyzed temperature and humidity from NOGAPS-ALPHA.

[39] Although *Merkel et al.* [2009] also utilized CIPS data to study the 5 day wave in PMC, there are significant differences between their results and those presented here. The main difference is a significantly lower 5 day PMC modulation seen in the late season by *Merkel et al.* [2009]. These differences are likely due to the fact that *Merkel et al.* [2009] utilized cloud albedo, whereas our study utilizes cloud frequency. Clouds are brighter during the main PMC season when a 5 day temperature signal will cause a significantly larger albedo response (as evident from the saturation plot in Figure 4c). In contrast, the cloud frequency does not distinguish between bright or faint clouds and is therefore more suitable for study of late-season wave modulation of PMCs. One must be cautious in interpreting the midseason wave signals, as high occurrence frequency (near 100%) will mask out any wave signal. Furthermore, a 5 day modulation will have more impact during periods of low-frequency cloud occurrence as compared to periods of high cloud occurrence. This seasonal variability in the variance reference point for both cloud albedo and occurrence frequency illustrates the importance of considering both cloud parameters when addressing seasonal variations in large-scale wave dynamics in the PMC field.

[40] Figure 9 shows time series of the band-passed 5 day wave oscillation in CIPS PMC occurrence (dashed line) and NOGAPS-ALPHA temperature (solid line) at two longitudes (270°E and 90°E) in the 75°N–85°N latitude band, which illustrate the phase relation between the two fields. The phase difference varies considerably and exhibits both in- and out-of-phase relations. However, during the late season the PMC occurrence and temperature both show strong 5 day signals that are nearly anticorrelated, with the peak in PMC occurrence leading the temperature trough slightly. Again, this provides further support of the dominant influence the 5 day temperature wave has on the late-season PMC field.

[41] As the examples shown in Figure 9 are representative of the phase relation, we show in Figure 10 the band-passed 5 day squared wavelet cross-coherence between CIPS cloud frequency and NOGAPS-ALPHA temperature, defined as [e.g., *Torrence and Webster*, 1999; *Grindsted et al.*, 2004]

$$L_{T,\mathrm{CIPS}}^2 = \frac{\left| \alpha \left(a^{-1} W_T \cdot W_{\mathrm{CIPS}}^* \right) \right|^2}{\alpha \left(a^{-1} |W_T|^2 \right) \cdot \alpha \left(a^{-1} |W_{\mathrm{CIPS}}|^2 \right)}, \qquad (2)$$

where W_T is the temperature wavelet transform and W_{CIPS}^* is the complex conjugate of the wavelet transform of CIPS PMC occurrence. The cross-coherence, which is the normalized form of the standard cross-spectrum, involves smoothing in both time and scale [e.g., *Ge*, 2008]. In our study, we have used the Morlet wavelet smoothing operator, α, as defined by *Torrence and Webster* [1999] and *Grindsted et al.* [2004]. Large L^2 helps to locate periods of time (for a given scale) where the two time series are highly correlated but do not
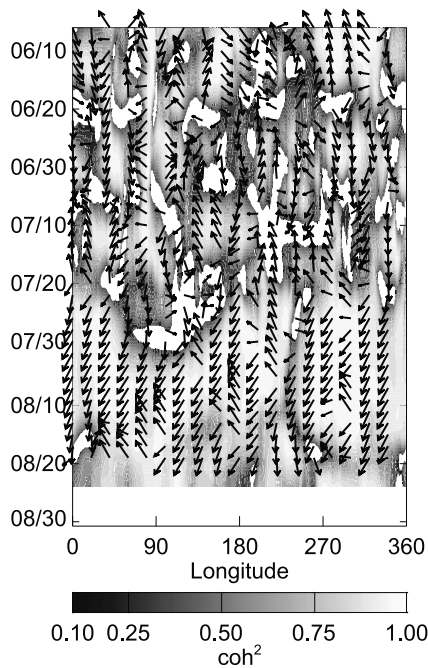
Figure 10. Filtered 5 day wavelet cross-coherence squared between NOGAPS-ALPHA temperature and CIPS cloud frequency shown in Figures 7 and 8. The phase differences between the two wave signals are illustrated by arrows: right arrows show in phase, left arrows indicate out of phase, while up (down) arrows illustrate CIPS cloud occurrence leading (trailing) temperature by 90°. In this figure, only values above the 95% significance level are drawn.

necessarily both exhibit enhanced levels of variance. Figure 10 only contours those regions above the 95% significance level, as determined using the wavelet-based methodology of *Ge* [2008].

[42] During the main PMC season, the squared cross-coherence in Figure 10 is dominated by localized regions of both low and high values. In contrast, the later part of the season is dominated by high cross-coherences due to a phase-locked relationship between the 5 day signals in NOGAPS-ALPHA temperature and CIPS cloud occurrence frequency. The phase difference, provided by the cross-spectral phase, is depicted in Figure 10 by arrows, with in phase illustrated by a right oriented arrow and out of phase by a left oriented arrow. A downward (upward) pointed arrow shows CIPS PMC frequency leading (lagging) NOGAPS-ALPHA temperature by 90°. The season exhibits a complex phase relationship with differences spanning both in- and out-of-phase relations. However, during August, when the 5 day wave is strongest, the majority of the phase arrows shows an overall tendency for the cloud frequency to lead the temperature by ~150°. This is equivalent to the clouds exhibiting a peak ~30° (~10 hours) prior to the temperature minimum and is in good agreement with the results found by *Merkel et al.* [2008] using PMC observations from the Student Nitric Oxide Explorer (SNOE) experiment and SABER temperature. Most recently, *Merkel et al.* [2009] reported a temperature-PMC phase relationship varying from 150° to 180° based on 5 day waves in CIPS

albedo and SABER temperature during the main 2007 PMC season (their analysis ended 14 July due to the SABER yaw maneuver), although *Merkel et al.* [2009, Figure 9] also exhibited appreciable phase variability (80°–180°) within their 5 day bandwidth. They suggested that these phase differences may be the result of a 5 day signal in water vapor exhibiting a phase different to that in temperature.

[43] To investigate this in detail, Figure 11 plots the squared wavelet cross-coherence between the NOGAPS-ALPHA temperature and water vapor mixing ratio. The temperature–water vapor squared cross-coherence exhibits similar behavior to the temperature-CIPS squared cross-coherences with localized regions of both low and high values. However, the uniformly high squared cross-coherences seen in Figure 10 after 25 July are not evident to the same degree in Figure 11 and may be due to the small 5 day humidity variance in August (Figure 7b), whereas both temperature and CIPS experienced a significant increase in 5 day wavelet variance (see Figures 7a and 8b, respectively). The phase relationship exhibited in regions of high cross-coherence within the time period of 25 July to 10 August shows a great deal of variability, pointing toward a variable phase relationship rather than the relatively straightforward relationship seen in Figure 10.

[44] To further address the phase relations among the 5 day wave responses in temperature, water vapor, and cloud frequency, Figure 12 plots 5 day band-passed oscillations in temperature (solid line), water vapor (dotted line), saturation ratio (dashed line), and CIPS PMC occurrence (dash-dotted line) at three different longitudes. The time series at 340°E longitude in Figure 12a are characterized by relatively strong temperature perturbations (around ±2 K) and some of the largest variations in water vapor (up to ±0.25 ppmv)
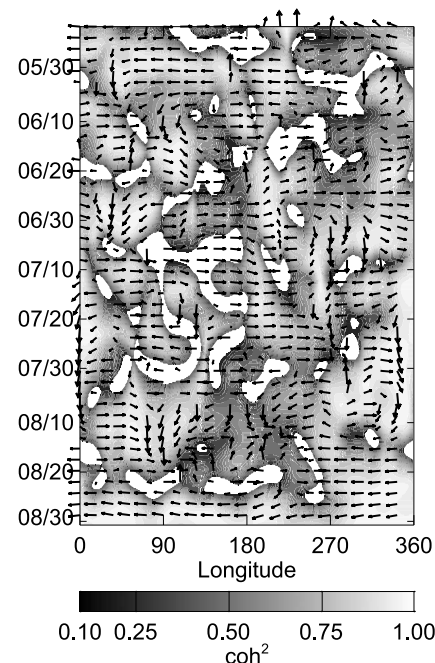

Figure 11. As in Figure 10, but now showing the squared cross-coherence between NOGAPS-ALPHA temperature and water vapor.
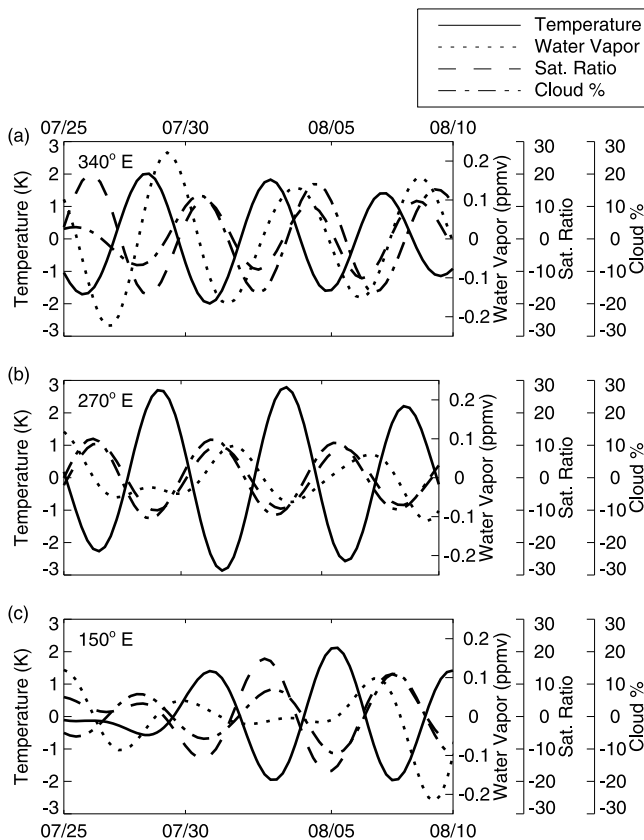
Figure 12. Band-passed quasi 5 day time series of NOGAPS-ALPHA temperature (solid lines), water vapor (dotted lines), saturation (dashed line), and CIPS cloud frequency (dash-dotted lines) during the late polar mesospheric cloud (PMC) season from 25 July to 10 August at three different longitudes: (a) 340°E, (b) 270°E, and (c) 150°E. These longitudes were chosen to illustrate the varying phase relations among 5 day signals in temperature, saturation, and cloud frequency.

associated with the 5 day wave. The time series at this longitude also exhibit the highest squared cross-coherences between temperature and water vapor, and between temperature and CIPS PMC occurrence. Hence, this longitude is ideal for determining potential effects of phase differences between temperature and water vapor on the cloud occurrence frequency. The time series at 270°E in Figure 12b are characterized by large-amplitude temperature perturbations (~3 K) but modest variations in water vapor, while at 150°E (Figure 12c) both the temperature and water vapor fields exhibit varying amplitudes with relatively low values of squared cross-coherence. The plots only show the late season, when the strongest 5 day wave signals are observed.

[45] In Figure 12a the temperature and water vapor are phase locked, which is also reflected in the high values of cross-coherence (~1) at this longitude, with water vapor leading the temperature by ~60°. The temperature and cloud occurrence exhibit a near phase-locked antiphase relation with the clouds peaking ~15° (or 5 hours) prior to the temperature troughs. The saturation ratio to a large degree follows the temperature in an antiphase relation. However, the

two parameters are not phase locked. Their phase difference varies considerably, with the saturation peak initially leading the temperature trough to later trailing by as much as 90°, such that the peak in saturation is "pulled" toward the water vapor peak. However, the clear phase-locked relation between water vapor and temperature as compared to the varying phase relation between saturation and temperature strongly suggest that the variations of both temperature and water vapor must impact 5 day signals in saturation. In Figure 12b with the stronger temperature variations, a strong antiphase (180°) relation arises between saturation and temperature that is clearly correlated with the cloud frequency. There is a small shift in phase such that the saturation trails the CIPS peak by up to ~15° or 5 hours. The variation in water vapor is small and does not exhibit a pattern that is as clear as that seen in temperature. Furthermore, the water vapor signal shows no sign of causing a varying phase shift between temperature and saturation ratio. Figure 12c shows varying amplitudes in temperature and water vapor, with relatively low absolute values of cross-coherence between the two fields. This case is interesting as it shows a varying phase relationship between temperature and saturation despite almost no signal in water vapor. Since the saturation is directly derived from temperature and water vapor, this observation likely reflects the fact that the late-season 5 day saturation signal is insignificant in comparison to midseason values.

[46] In order to better understand the individual contributions, Figure 13 plots the saturation ratio calculated using equation (1) under various idealized environmental conditions covering a 20 day period with a temperature background of 145 K and a water vapor background of 5 ppmv,
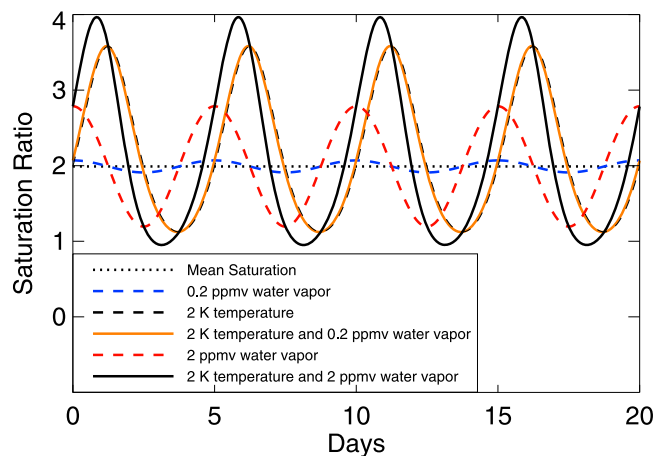

Figure 13. Saturation ratio calculated using equation (1) using different 5 day temperature and water vapor mixing ratio conditions based on values in Figure 12. The background saturation is shown by the black dotted line. The saturation based on a 5 day water vapor wave of 0.2 ppmv amplitude is shown with a blue dashed line, while the black dashed line shows the saturation for a pure 2 K temperature amplitude. The saturation for the 0.2 ppmv and 2 K signals combined is shown in orange. A 2 ppmv water vapor amplitude yields the dashed red curve, while the black line represents the saturation for a 2 K temperature and a 2 ppmv water vapor amplitude.

resembling mean conditions toward the end of July. The dotted line shows the mean saturation value of 2. The black dashed line shows the saturation ratio based on a pure 5 day wave temperature signal with an amplitude of 2 K, while the blue dashed curve shows the saturation signal caused by a 5 day water vapor oscillation of 0.2 ppmv amplitude (phase shifted with respect to the temperature wave). Both amplitudes and phases are chosen based on Figure 12a. The solid orange line shows saturation when the temperature and water vapor signals are combined. It is evident that at these amplitudes, the saturation signal is dominated by the temperature variations. It would require an increase in the water vapor amplitude to 2 ppmv (dashed red curve) to produce a phase shift in the saturation when combined with a 2 K temperature wave (solid black curve).

[47] The 5 day water vapor amplitudes in the NOGAPS-ALPHA analysis lie well below this 2 ppmv value and thus cannot explain the phase shift between NOGAPS-ALPHA 5 day temperature and saturation, indicating that an adequate estimation of the saturation amplitude by the wavelet analysis is not obtained. As discussed by *Eckermann et al.* [2009], the coarse vertical resolution of the MLS water vapor observations probably attenuates the 5 day wave structure in water vapor, causing an underestimate of the water vapor signal in our analysis. According to the above analysis, the suppressed signal is not adequate to fully address the impact of water vapor on the varying phase relationship between temperature and cloud occurrence frequency. Our analysis shows that a 10-fold increase in 5 day wave–induced humidity anomalies is needed to cause a large phase shift between 5 day wave phases in saturation and temperature, that is sufficient to explain the observed phase shift between 5 day signals in CIPS cloud occurrence frequency and NOGAPS-ALPHA temperature.

4. Discussion

[48] Our observations of increased 5 day wave activity in August are consistent with the observations reported by *Beard et al.* [2001] from a single midlatitude station (53°N). They showed a surge in planetary wave activity toward the end of the boreal summer, with bursts of transient activity. The late surge was attributed to the fact that the prevailing middle atmospheric westward wind jet transitions to eastward near the equinox, increasing the possibility of upward propagation of planetary waves from the troposphere. They also reported significant migration of the wave periods during the course of the season caused by Doppler shifting of the wave frequencies by the background wind. Other observations closer to equinox have shown large-amplitude planetary wave perturbations, linked to the reversal of the zonal mean winds. The resultant surge of planetary waves propagating into the mesosphere [e.g., *Liu et al.*, 2001; *Lieberman et al.*, 2003] can cause temperature anomalies as large as 25–30 K [*Taylor et al.*, 2001]. Although our period of interest is ~6 weeks prior to the fall equinox, the initial weakening of the wind field is in progress and may allow occasional wave penetration into the MLT. Significant enhancements in mesospheric large-scale wave activity outside the equinox have also been reported previously and attributed to an unstable atmospheric mode [*Meyer and Forbes*, 1997], nonlinear wave interaction between a 7 day,

wave number 2 planetary wave and a stationary planetary wave (wave nummber 1) resulting in a secondary normal mode [*Pogoreltsev et al.*, 2002], and amplification through baroclinic instability of a normal mode [*Plumb*, 1983; *Garcia et al.*, 2005; *Riggin et al.*, 2006]. Baroclinic instability also drives significant planetary wave amplification above 80 km during the fall equinox transition period [*Lieberman et al.*, 2003].

[49] To assess possible wave amplification through baroclinic instability, we use the NOGAPS-ALPHA analysis fields to calculate the meridional derivative of zonally averaged potential vorticity given by [e.g., *Andrews et al.*, 1987]

$$\frac{\partial \overline{q}}{\partial y} = \beta - \frac{\partial^2 \overline{u}}{\partial y^2} - \frac{1}{\rho_0} \frac{\partial}{\partial z} \left(\rho_0 \epsilon \frac{\partial \overline{u}}{\partial z} \right), \quad (3)$$

where $\overline{u}$ is the zonal mean zonal wind, ρ_0 is the atmospheric density, and ϵ is given by the squared ratio between the Coriolis parameter $f = 2\Omega \sin \psi$ and the buoyancy frequency N,

$$\epsilon = \frac{f^2}{N^2}, \quad (4)$$

and β is the planetary vorticity gradient given by

$$\beta = \frac{2\Omega \cos \psi}{a}. \quad (5)$$

Here Ω is the angular frequency of the Earth, ψ is latitude, and a is Earth radius. In the calculations that follow, we will adopt constant values of f and β and restrict our analysis to a limited latitude range to be consistent with a β plane approximation. We also adopt constant N to focus on the more important vertical variations in $\overline{u}$.

[50] The requirement for baroclinic instability is negative $\partial \overline{q}/\partial y$ arising from vertical shear of the mean zonal flow [e.g., *Andrews et al.*, 1987; *Holton*, 1992]. Figure 14 shows $\partial \overline{q}/\partial y$ for the periods of 1–10 July and 1–10 August covering the latitude band 40°N–80°N, with $\overline{u}$ shown by the black contours.

[51] It is evident that the region between 0.1 and 0.01 hPa is baroclinically unstable at these times. However, a comparison of Figures 14a and 14b shows that the higher latitudes in August are more unstable than in July, with instability peaking at 0.01 hPa and 60°N–65°N, coincident with a relatively steep vertical gradient in $\overline{u}$. With this information in mind, we may expect greater local wave forcing in August as compared to July. This amplification can be seen in Figure 15, which shows an altitude vs. longitude cross section (averaged over 65°N–75°N) of the daily averaged 5 day wave temperature amplitude for 5 August. At altitudes below 0.01 hPa, the wave amplitude is moderate (<2 K). However, the wave amplitude is significantly larger just above the region of maximum instability. The two dashed lines in Figure 15 indicate the PMC altitude boundaries used in this paper (~82–87 km) and show the 5 day wave peaking near the top PMC level considered in our study.

[52] The traditional 5 day wave observed in the mesosphere near the fall equinox is an upward propagating disturbance and penetration of this wave into the mesopause
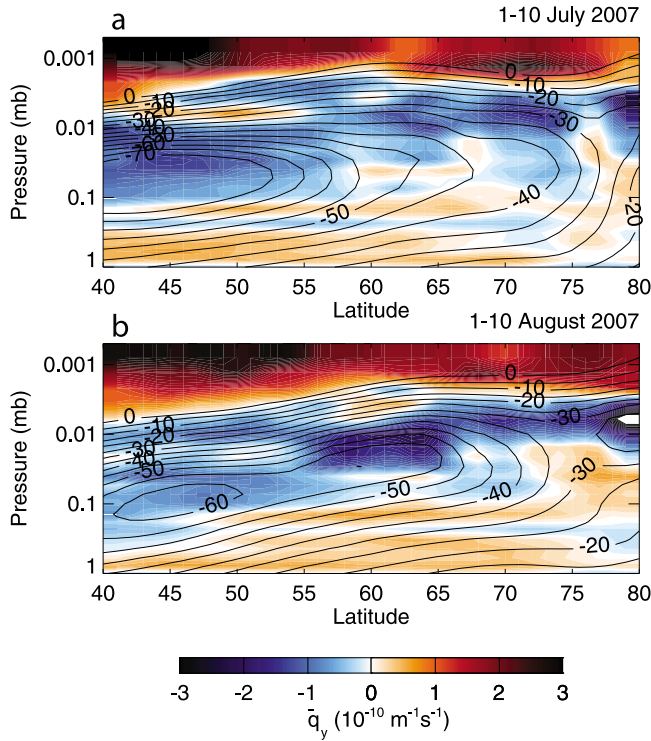
Figure 14. Meridional gradient of zonally averaged potential vorticity for (a) 1–10 July and (b) 1–10 August from the NOGAPS-ALPHA analysis. The zonal mean zonal wind is shown by the contour lines, with contour labels in m s^{-1}.

region is facilitated by the weaker winds during the equinox as compared to summer [e.g., *Lieberman et al.*, 2003]. As the zonal wind reversal is in progress in August, it is plausible that transient mean wind vacillations may allow for penetration of the 5 day wave into the mesosphere. Another possible mechanism is wave generation in the unstable region shown in Figure 14 [e.g., *Meyer and Forbes*, 1997]. To determine the genesis of the wave disturbance seen in our data, we compute Eliassen-Palm (EP) flux vectors, which quantify intrinsic wave activity and can also be utilized as a diagnostic of wave propagation [e.g., *Andrews et al.*, 1987]. The EP flux due to the 5 day disturbance calculated on a quasi-geostrophic β plane is [e.g., *Andrews et al.*, 1987]

$$\vec{F} = \left(0, -\rho\overline{v'u'}, \rho f\overline{v'\theta'}/\overline{\theta}_z\right). \tag{6}$$

Here v is the meridional wind component, $\overline{\theta}$ is the background potential temperature, primes denotes perturbations due to the 5 day wave, subscript z denotes the partial derivative with respect to altitude, and overbars denote averages around a latitude circle.

[53] The contours in Figure 16 show the zonal mean zonal wind for 3–5 July (Figure 16, top) and 3–5 August (Figure 16, bottom) (recall that the peak 5 day amplitude in temperature occurred during this latter period in August) with solid and dashed lines indicating eastward and westward winds, respectively. Regions of $\partial\overline{q}/\partial y < 0$ are shaded grey. The thick grey line shows the critical level for the 5 day wave

where the wave phase speed matches the background flow and thus prohibits vertical wave propagation. For planetary waves the phase speeds (assuming a wave number 1 disturbance) are

$$c = \frac{2\pi a \cos \psi}{\tau}, \tag{7}$$

where τ is the ground-based wave period. The EP fluxes are plotted in Figure 16 with black arrows and an arrow to scale is shown in the upper left of Figure 16b. During the July period, Figure 16a shows evidence for an upward propagating wave disturbance near 50°N–55°N at the 1 hPa level. However, the disturbance cannot penetrate above the 0.1 hPa level where it approaches a critical level. The upper mesosphere shows little evidence of wave activity. In contrast, the August period in Figure 16b is dominated by significantly larger eddy heat fluxes ($\overline{v'\theta'}$) near PMC altitudes of 0.006 hPa, which increase significantly in the region characterized by negative $\partial\overline{q}/\partial y$ (compare Figure 14). These observations suggest that enhanced 5 day wave amplitudes at PMC altitudes in August arose due to wave generation from baroclinic instabilities in the mesosphere. Furthermore, there is little evidence of a 5 day planetary wave propagating upward from the lower atmosphere as there are critical levels in the intervening atmosphere that should inhibit penetration of such waves into the mesosphere. Our findings agree with *Liu et al.* [2004], who found maximum 5 day wave amplitude before and after the equinoxes, possibly due to baroclinic instabilities.

[54] The increased 5 day wave amplitudes we have observed here in late summer may have a connection with ground-based NLC observations. Note that high-latitude passive ground-based optical observations are often impacted during midsummer by limited nighttime hours for observation. Optimal viewing conditions do not occur until early August when, interestingly, surprisingly bright and pervasive NLC displays occur. Lidar observations also often show bright
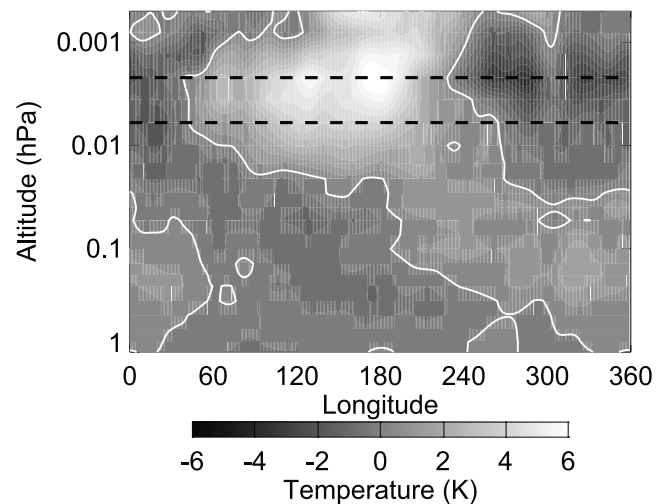

Figure 15. Longitude-height cross section of the temperature 5 day wave on 5 August 2007, averaged over the 65°N–75°N latitude band. The dashed lines represent the PMC altitude range considered in this paper (~82–87 km).
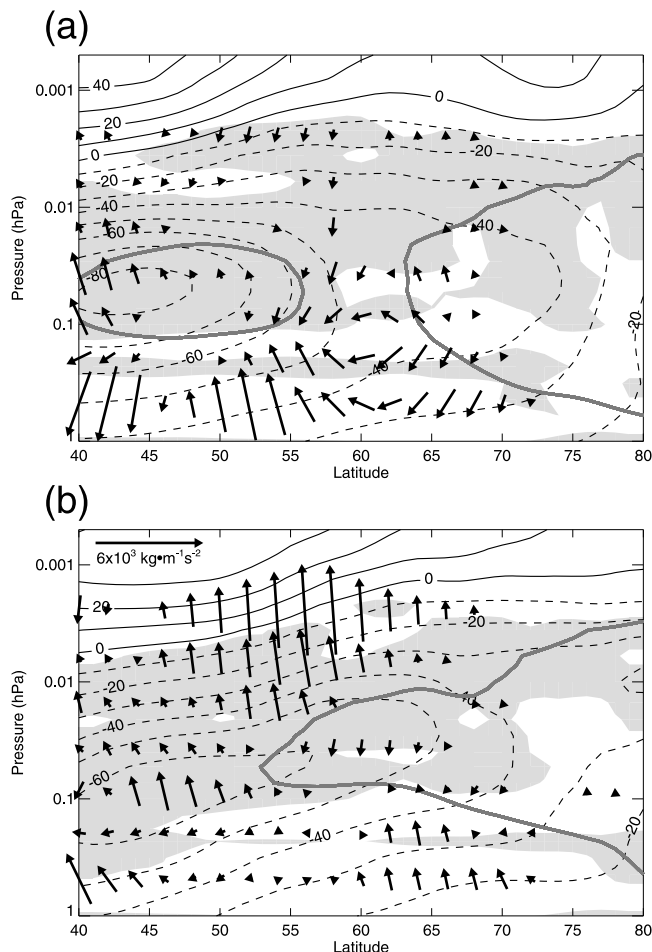
Figure 16. Zonal mean zonal wind (contours with westward wind shown as dashed contours and eastward wind shown as solid contours, with contour labels in m s^{-1}), 5 day wave critical level (bold shaded contours), negative $\partial\overline{q}/\partial y$ (shaded), and Eliassen–Palm flux illustrated by the vector field for the periods (a) 3–5 July and (b) 3–5 August.

ratio for the 60°N–65°N latitude band for the 2007 summer. It is evident that the core of the 2007 PMC season at these latitudes, based solely on regions of widespread zonal mean saturation, extends from early June to around 15 July. However, the plot also shows significant levels of saturated air as a result of the 5 day wave in early August, suggesting that at these latitudes, the 5 day wave can indeed extend the PMC season beyond what is expected from zonal mean conditions alone.

5. Conclusion

[56] We have used assimilated meteorological fields from the NOGAPS-ALPHA system to investigate the evolution of the quasi 5 day wave during the first AIM PMC season, covering the period from 15 May to 31 August 2007. In particular, we investigated the 5 day wave in assimilated temperature, water vapor, and derived saturation ratio fields, and explored how it related to PMCs observed by the SOFIE and CIPS instruments on board AIM. The wave showed a significant enhancement in the late PMC season (early August) with coherent wave 1 temperature structure extending across all longitudes. In contrast, the water vapor wavefield exhibited a fairly uniform wave amplitude throughout the season.

[57] A comparison between NOGAPS-ALPHA wavefields and the corresponding PMC signatures in CIPS revealed that 5 day wave–induced variations in temperature, saturation, and cloud frequency exhibited a variety of phase relations during the mid-PMC season in concert with the findings of *Merkel et al.* [2009]. However, during the 5 day wave burst
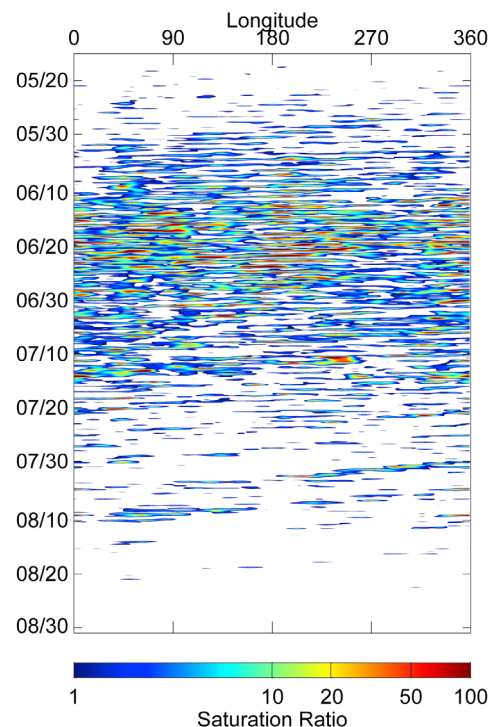
NLCs in early August [*Collins et al.*, 2003, 2009]. Most recently, *Collins et al.* [2009] reported the strongest NLC signal detected to date at Poker Flat Research Range, Alaska (65°N) observed using a Rayleigh lidar on 9 August 2005. The NLC field was also detected by digital cameras and showed extensive displays covering most of the northern horizon and covering the camera's field of views [*Collins et al.*, 2009]. Interestingly, and similar to our results, *von Savigny et al.* [2007, Figure 5] clearly shows the strongest 5 day temperature amplitude in 2005 occurred in August. Furthermore, their PMC wavelet power spectrum exhibited peaks in early August coincident with the temperature perturbations. This suggests that the NLC observations of *Collins et al.* [2009] potentially were caused by a strong 5 day temperature wave. However, *von Savigny et al.* [2007] considered a broad latitude band extending from 60°N–80°N and the PMC 5 day signal may be dominated by contributions from the high latitudes.

[55] To test our hypothesis regarding the 5 day wave control of late-season PMC formation at these lower polar latitudes, Figure 17 plots the NOGAPS-ALPHA saturation

Figure 17. Hovmöller plot of NOGAPS-ALPHA saturation ratio averaged over the 60°N–65°N latitude range and 0.006–0.0022 hPa (~82–87 km) range.

in August, the responses exhibited coherent phase-locked relationships, with the peak PMC response occurring ~5–10 hours prior to peak in the 5 day wave–induced cold temperatures and saturation when relatively strong temperature perturbations (~3 K) were present. Our study also showed that the 5 day water vapor signal was of insufficient amplitude to distort the phase-locked relation between temperature and saturation. A simple model study showed that an order of magnitude increase in the 5 day water vapor amplitude is needed to cause a significant phase difference between 5 day signals in temperature and saturation. Owing to the coarse vertical resolution and random errors in the assimilated MLS humidity observations at PMC altitudes, the 5 day water vapor amplitude was likely underestimated. Thus the hypothesis of *Merkel et al.* [2009], that the 5 day wave signal in water vapor might explain the variable phase relations between 5 day wave–induced signals in temperature and clouds, requires further investigation.

[58] A study of bright clouds measured by SOFIE showed them preferentially forming in the cold phase of the 5 day wave during both the cold peak PMC season and, in particular, toward the end of the season as suggested by previous studies [e.g., *von Savigny et al.*, 2007]. Together, these results strongly point to the late-season 2007 PMC observations being driven by a large-amplitude 5 day planetary wave oscillation. This oscillation provided regions favorable for PMC formation well into August despite a zonal mean saturation environment which, after 25 July, was marginal for cloud existence.

[59] Utilizing winds derived from the assimilation, we found that the early end-of-season transition in the zonal mean winds produced a baroclinically unstable region in the middle atmosphere at ~0.1–0.01 hPa, which generated large upward propagating 5 day wave EP fluxes. We postulate that this late summer transition in the zonal wind increases the likelihood of large-amplitude 5 day wave activity in the summer mesosphere and may explain the surprising brightness of numerous NLCs observed from the ground in early August in 2007 and in earlier years.

Appendix

[60] The Morlet wavelet basis function is a complex sinusoidal waveform with a Gaussian envelope given by

$$\Psi(\eta) = \frac{1}{\pi^{-1/4}} \cdot e^{i\omega_0\eta}e, \qquad (A1)$$

where ω_0 is the dimensionless central frequency of the wavelet and η is dimensionless time. The choice of $\omega_0 = 6$ provides an adequate balance between time and frequency localizations [e.g., *Torrence and Compo*, 1998; *Grindsted et al.*, 2004]. The continuous wavelet transform of a time-dependent signal, *x(t)*, is defined as

$$W(a,b) = \frac{1}{\sqrt{a}} \int_{-\infty}^{\infty} x(t) \cdot \Psi^*\left(\frac{t-b}{a}\right) dt, \qquad (A2)$$

where the asterisk denotes the complex conjugate and *a* is the dilation parameter that governs the scaling of the wavelet. The sliding of the wavelet in time is determined by the location parameter (or localized time index) *b*. For a specific scale, *a*, the wavelet slides through the time series

(increasing *b*) identifying localized regions with structures relating to the scale. This process is repeated over the specified range of scales.

[61] Equation (A2) is also the convolution of the basis wavelet function through the time signal. For practical reasons, it is convenient to apply the Fourier convolution theorem to write the wavelet transform as the product of the wavelet and signal Fourier transforms:

$$W(a,b) = \int \int_{-\infty}^{\infty} \frac{1}{\sqrt{a}} \cdot \hat{x}(f) \cdot \hat{\Psi}^*\left(\frac{t-b}{a}\right) \cdot \exp[\iota(2\pi ft)] \, dt \, df. \qquad (A3)$$

Here hatted symbols denote the Fourier transformed signals and *f* is the characteristic frequency associated with a wavelet of scale *a*.

[62] The above expression can be written as

$$W(a,b) = \sqrt{a} \int_{-\infty}^{\infty} \hat{x}(f) \cdot \hat{\Psi}^*(af) \cdot \exp[\iota(2\pi f)b] \, df, \qquad (A4)$$

where *af* is a rescaled frequency. Equation (A4) has the same form as an inverse Fourier transform. Hence, we can utilize a fast Fourier transform algorithm to calculate the wavelet transform, providing we use a discrete approximation of the continuous wavelet transform.

[63] The wavelet transform, *W(a, b)*, is complex and the contribution of signal energy from a specific scale *a* and location (time) *b* is contained in the two-dimensional wavelet energy density function (or wavelet power spectrum) defined as $|W(a, b)|^2$. The wavelet amplitude is $|W(a, b)|$ and the phase is given by $\tan^{-1}(W_i/W_r)$, where subscripts denote the imaginary and real parts of the wavelet transform [e.g., *Torrence and Compo*, 1998; *Grindsted et al.*, 2004; *Addison*, 2002].

[64] In our study, we have also used the wavelet transform as a band-pass filter to capture the 5 day signal using a bandwidth ranging from 4.1 to 6.5 days. The scale-averaged wavelet variance is a weighted sum of the power over the scales, *a*, contained within the bandwidth and is given by [e.g., *Torrence and Compo*, 1998]

$$W^2 = \frac{\delta j \delta t}{C_\delta} \sum_{i=m}^{n} \frac{\left|W(a_i,b)^2\right|}{a_i}, \qquad (A5)$$

where the summation is over each scale within the determined bandwidth, bounded by scales a_m and a_n. The average signal amplitude is given by

$$W = \frac{\delta j \delta t^{1/2}}{C_\delta \Psi_0(0)} \sum_{i=m}^{n} \frac{W_r(a_i,b)}{a_i^{1/2}}. \qquad (A6)$$

[65] The constants depend on the mother wavelet used and the temporal resolution in the time series. In our analysis $\delta j = 1/8$, $\delta t = 0.25$, $C_\delta = 0.776$ and $\Psi_0(0) = \pi^{-1/4}$. For more detailed information on wavelet analysis, see, for example, *Kaiser* [1994], *Addison* [2002], and *Torrence and Compo* [1998].

References

Addison, P. S. (2002), *The Illustrative Wavelet Transform Handbook*, Taylor and Francis, New York.

Ahlquist, J. E. (1982), Normal-mode global Rossby waves: Theory and observations, *J. Atmos. Sci.*, 39, 193–202.

Andrews, D. G., J. R. Holton, and C. B. Leroy (1987), *Middle Atmospheric Dynamics*, Academic, Orlando, Fla.

Azeem, S. M. I., S. E. Palo, D. L. Wu, and L. Froidevaux (2001), Observations of the 2-day wave in UARS MLS temperature and ozone measurements, *Geophys. Res. Lett.*, 28, 3147–3150.

Baker, N. L., et al. (2007), An overview of the NRL Atmospheric Variational Data Assimilation (NAVDAS) and NAVDAS-AR (Accelerated Representer) systems, paper 2B.1 presented at the 18th Conference on Numerical Weather Prediction, Am. Meteorol. Soc., Park City, Utah, 25–29 June.

Beard, A. G., P. J. S. Williams, N. J. Mitchell, and H. G. Muller (2001), A special climatology of planetary waves and tidal variability, *J. Atmos. Sol. Terr. Phys.*, 63, 801–811, doi:10.1016/S1364-6826(00)00194-2.

Benze, S., C. E. Randall, M. T. DeLand, G. E. Thomas, D. W. Rusch, S. M. Bailey, J. M. Russell III, W. E. McClintock, A. W. Merkel, and C. Jeppesen (2009), Comparison of polar mesospheric cloud measurements from the cloud imaging and particle size experiment and the solar backscatter ultraviolet instrument in 2007, *J. Atmos. Sol. Terr. Phys.*, 71, 365–372, doi:10.1016/j.jastp.2008.07.014.

Collins, R. L., M. C. Kelley, M. J. Nicolls, C. Ramos, T. Hou, T. E. Stern, K. Mizutani, and T. Itabe (2003), Simultaneous lidar observations of a noctilucent cloud and an internal wave in the polar mesosphere, *J. Geophys. Res.*, 108(D8), 8435, doi:10.1029/2002JD002427.

Collins, R. L., M. J. Taylor, K. Nielsen, K. Mizutani, Y. Murayama, K. Sakanoi, and M. T. DeLand (2009), Noctilucent cloud in the western Arctic in 2005: Simultaneous lidar and camera observations and analysis, *J. Atmos. Sol. Terr. Phys.*, 71, 446–452, doi:10.1016/j.jastp.2008.09.044.

Eckermann, S. D., K. W. Hoppel, L. Coy, J. P. McCormack, D. E. Siskind, K. Nielsen, A. Kochenash, M. H. Stevens, C. R. Englert, and M. E. Hervig (2009), High-altitude data assimilation system experiments for the northern summer mesosphere season of 2007, *J. Atmos. Sol. Terr. Phys.*, 71, 531–551, doi:10.1016/j.jastp.2008.09.036.

Forbes, J. M. (1995), Tidal and planetary waves, in *The Upper Mesosphere and Lower Thermosphere: A Review of Experiment and Theory*, *Geophys. Monogr. Ser.*, vol. 87, edited by R. M. Johnson and T. L. Killeen, pp. 67–87, AGU, Washington, D. C.

Garcia, R. R., R. Liebermann, J. M. Russell III, and M. G. Mlynczak (2005), Large-scale waves in the mesosphere and lower thermosphere observed by SABER, *J. Atmos. Sci.*, 62, 4384–4399, doi:10.1175/JAS3612.1.

Ge, Z. (2008), Significance tests for the wavelet cross spectrum and wavelet linear coherence, *Ann. Geophys.*, 26, 3819–3829.

Gordley, L. L., et al. (2009), The solar occultation for ice experiment, *J. Atmos. Sol. Terr. Phys.*, 71, 300–315, doi:10.1016/j.jastp.2008.07.012.

Grindsted, A., J. C. Moore, and S. Jevrejeva (2004), Application of the cross wavelet transform and wavelet coherence to geophysical time series, *Nonlinear Process. Geophys.*, 11, 561–566.

Hervig, M. E., L. L. Gordley, M. H. Stevens, J. M. Russell III, S. M. Bailey, and G. Baumgarten (2009), Interpretation of SOFIE PMC measurements: Cloud identification and derivation of mass density, particle shape, and particle size, *J. Atmos. Sol. Terr. Phys.*, 71, 316–330, doi:10.1016/j.jastp.2008.07.009.

Hirooka, T. (2000), Normal mode Rossby waves as revealed by UARS/ISAMS observations, *J. Atmos. Sci.*, 57, 1277–1285, doi:10.1175/1520-0469(2000).

Holton, J. R. (1992), *An Introduction to Dynamic Meteorology, Int. Geophys. Ser.*, vol. 48, Academic, San Diego, Calif.

Hoppel, K. W., N. L. Baker, L. Coy, S. D. Eckermann, J. P. McCormack, G. E. Nedoluha, and D. E. Siskind (2008), Assimilation of stratospheric and mesospheric temperature from MLS and SABER into a global NWP model, *Atmos. Chem. Phys.*, 8, 6103–6116.

Kaiser, G. (1994), *A Friendly Guide to Wavelets*, Birkhäuser Boston, Cambridge, Mass.

Kirkwood, S., and K. Stebel (2003), Influence of planetary waves on noctilucent cloud occurrence over NW Europe, *J. Geophys. Res.*, 108(D8), 8440, doi:10.1029/2002JD002356.

Kirkwood, S., V. Barabash, B. U. E. Brändström, A. Moström, K. Stebel, N. Mitchell, and W. Hocking (2002), Noctilucent clouds, PMSE and 5-day planetary waves: A case study, *Geophys. Res. Lett.*, 29(10), 1411, doi:10.1029/2001GL014022.

Körner, U., and G. R. Sonnemann (2001), Global three-dimensional modeling of the water vapor concentration of the mesosphere-mesopause region and implications with respect to the noctilucent cloud region, *J. Geophys. Res.*, 106, 9639–9651.

Lawrence, A. R., and M. J. Jarvis (2003), Simultaneous observations of planetary waves from 30 to 220 km, *J. Atmos. Sol. Terr. Phys.*, 65, 765–777, doi:10.1016/S1364-6826(03)00081-6.

Lejenäs, H., and R. A. Madden (1992), Traveling planetary-scale waves and blocking, *Mon. Weather Rev.*, 120, 2821–2830, doi:10.1175/1520-0493.

Lieberman, R. S., D. M. Riggin, S. J. Franke, A. H. Manson, C. E. Meek, T. Nakamura, T. Tsuda, R. A. Vincent, and I. Reid (2003), The 6.5-day wave in the mesosphere and lower thermosphere: Evidence for baroclinic/barotropic instability, *J. Geophys. Res.*, 108(D20), 4640, doi:10.1029/2002JD003349.

Liu, H.-L., R. G. Roble, M. J. Taylor, and W. R. Pendleton Jr. (2001), Mesospheric planetary waves at Northern Hemisphere fall equinox, *Geophys. Res. Lett.*, 28, 1903–1906.

Liu, H.-L., E. R. Talaat, R. G. Roble, R. S. Lieberman, D. M. Riggin, and J.-H. Yee (2004), The 6.5-day wave and its seasonal variability in the middle and upper atmosphere, *J. Geophys. Res.*, 109, D21112, doi:10.1029/2004JD004795.

Madden, R. A. (1978), Further evidence of traveling planetary waves, *J. Atmos. Sci.*, 35, 1605–1618, doi:10.1175/1520-0469(1978)035<1605:FEOTPW>2.0.CO;2.

Madden, R. A., and P. Julian (1972), Further evidence of global-scale, 5-day pressure waves, *J. Atmos. Sci.*, 29, 1464–1469, doi:10.1175/1520-0469(1972)029<1464:FEOGSD>2.0.CO;2.

McClintock, W. E., D. W. Rusch, G. E. Thomas, A. W. Merkel, M. R. Lankton, V. A. Drake, S. M. Bailey, and J. M. Russell III (2009), The cloud imaging and particle size experiment on the Aeronomy of Ice in the Mesosphere mission: Instrument concept, design, calibration, and on-orbit performance, *J. Atmos. Sol. Terr. Phys.*, 71, 340–355, doi:10.1016/j.jastp.2008.10.011.

Merkel, A. W., G. E. Thomas, S. E. Palo, and S. M. Bailey (2003), Observations of the 5-day planetary wave in PMC measurements from the Student Nitric Oxide Explorer Satellite, *Geophys. Res. Lett.*, 30(4), 1196, doi:10.1029/2002GL016524.

Merkel, A. W., R. R. Garcia, S. M. Bailey, and J. M. Russell III (2008), Observational studies of planetary waves in PMCs and mesospheric temperature measured by SNOE and SABER, *J. Geophys. Res.*, 113, D14202, doi:10.1029/2007JD009396.

Merkel, A. W., D. W. Rusch, S. E. Palo, J. M. Russell III, and S. M. Bailey (2009), Mesospheric planetary wave activity inferred from AIM-CIPS and TIMED-SABER for the northern summer 2007 PMC season, *J. Atmos. Sol. Terr. Phys.*, 71, 381–391, doi:10.1016/j.jastp.2008.12.001.

Meyer, C. K., and J. M. Forbes (1997), A 6.5-day westward propagating planetary wave: Origin and characteristics, *J. Geophys. Res.*, 102, 26,173–26,178.

Murphy, D. M., and T. Koop (2005), Review of the vapour pressures of ice and supercooled water for atmospheric applications, *Q. J. R. Meteorol. Soc.*, 131, 1539–1565.

Nedoluha, G. E., R. M. Bevilacqua, R. M. Gomez, W. B. Waltman, and B. C. Hicks (1996), Measurements of water vapor in the middle atmosphere and implications for mesospheric transport, *J. Geophys. Res.*, 101, 21,183–21,193.

Palo, S. E., and S. K. Avery (1996), Observations of the quasi-two-day wave in the middle and lower atmosphere over Christmas Island, *J. Geophys. Res.*, 101, 12,833–12,846.

Pancheva, D. V., and N. J. Mitchell (2004), Planetary waves and variability of the semidiurnal tide in the mesosphere and lower thermosphere over Esrange (68°N, 21°E) during winter, *J. Geophys. Res.*, 109, A08307, doi:10.1029/2004JA010433.

Plumb, R. A. (1983), Baroclinic instability of the summer mesosphere: A mechanism for the quasi-two-day wave?, *J. Atmos. Sci.*, 40, 262–270, doi:10.1175/1520-0469(1983)040<0262:BIOTSM>2.0.CO:2.

Pogoreltsev, A. I., I. N. Fedulina, N. J. Mitchell, H. G. Muller, Y. Luo, C. E. Meek, and A. H. Manson (2002), Global free oscillations of the atmosphere and secondary planetary waves in the mesosphere and lower thermosphere region during August/September time conditions, *J. Geophys. Res.*, 107(D24), 4799, doi:10.1029/2001JD001535.

Rapp, M., and G. E. Thomas (2004), Modeling the microphysics of mesospheric ice particles: Assessment of current capabilities and basic sensitivities, *J. Atmos. Sol. Terr. Phys.*, 68, 715–744, doi:10.1016/j.jastp.2005.10.015.

Riggin, D. M., et al. (2006), Observations of the 5-day wave in the mesosphere and lower thermosphere, *J. Atmos. Sol. Terr. Phys.*, 68, 323–339, doi:10.1016/j.jastp.2005.05.010.

Rosenlof, K. H., and R. J. Thomas (1990), Five-day mesospheric waves observed in solar mesospheric explorer ozone, *J. Geophys. Res.*, *95*, 895–899.

Rusch, D. W., G. E. Thomas, W. E. McClintock, A. W. Merkel, S. M. Bailey, J. M. Russell III, C. E. Randall, C. Jeppesen, and M. Callan (2009), The cloud imaging and particle size experiment on the Aeronomy of Ice in the Mesosphere mission: Cloud morphology for the northern 2007 season, *J. Atmos. Sol. Terr. Phys.*, *71*, 356–364, doi:10.1016/j.jastp.2008.11.005.

Russell, J. M., III, et al. (2009), Aeronomy of Ice in the Mesosphere (AIM): Overview and early science results, *J. Atmos. Sol. Terr. Phys.*, *71*, 289–299, doi:10.1016/j.jastp.2008.08.011.

Salby, M. L. (1984), Survey of planetary scale traveling waves: The state of theory and observations, *Rev. Geophys.*, *22*, 209–236.

Seele, C., and P. Hartogh (1999), Water vapor of the polar middle atmosphere: Annual variation and summer mesosphere conditions as observed by ground-based microwave spectroscopy, *Geophys. Res. Lett.*, *26*, 1517–1520.

Sonnemann, G. R., P. Hartogh, M. Grygalashvyly, S. Li, and U. Berger (2008), The quasi 5-day signal in the mesospheric water vapor concentration at high latitudes in 2003: A comparison between observations at ALOMAR and calculations, *J. Geophys. Res.*, *113*, D04101, doi:10.1029/2007JD008875.

Speth, P., and R. A. Madden (1983), Space-time spectral analyses of Northern Hemisphere geopotential heights, *J. Atmos. Sci.*, *40*, 1086–1100, doi:10.1175/1520-0469(1983)040<1086:STSAON>2.0.CO;2.

Stull, R. B. (1999), *Meteorology for Scientists and Engineers*, 2nd ed., Brooks Cole, Pacific Grove, Calif.

Taylor, M. J., W. R. Pendleton Jr., H.-L. Liu, C. Y. She, L. C. Gardner, R. G. Roble, and V. Vasoli (2001), Large amplitude perturbations in meso-spheric OH Meinel and 87-km Na lidar temperatures around the autumnal equinox, *Geophys. Res. Lett.*, *28*, 1899–1902.

Torrence, C., and G. P. Compo (1998), A practical huide to wavelet analysis, *Bull. Am. Meteorol. Soc.*, *79*, 61–78.

Torrence, C., and P. J. Webster (1999), Interdecadal changes in the ENSO-monsoon system, *J. Clim.*, *12*, 2679–2690, doi:10.1175/1520-0442 (1999)012<2679:ICITEM>2.0.CO;2.

Turnbridge, V. M., and N. J. Mitchell (2009), The two-day wave in the Antarctic and Arctic mesosphere and lower thermosphere, *Atmos. Chem. Phys.*, *9*, 6377–6388.

Volland, H. (1988), *Atmospheric Tidal and Planetary Waves*, Springer, London.

von Savigny, C., C. Roberts, H. Bovensmann, J. P. Burrows, and M. Schwartz (2007), Satellite observations of the quasi 5-day wave in noctilucent clouds and mesopause temperatures, *Geophys. Res. Lett.*, *34*, L24808, doi:10.1029/2007GL030987.

S. Benze and C. E. Randall, Laboratory for Atmospheric and Space Physics and Department of Atmospheric and Oceanic Sciences, University of Colorado at Boulder, 392 UCB, Boulder, CO 80309-0392, USA.

L. Coy, S. D. Eckermann, J. P. McCormack, and D. E. Siskind, Space Science Division, Code 7646, Naval Research Laboratory, 4555 Overlook Ave., SW, Washington, DC 20375, USA.

M. E. Hervig, GATS Inc., Driggs, ID 83422, USA.

K. W. Hoppel, Remote Sensing Division, Code 7200, Naval Research Laboratory, 4555 Overlook Ave., SW, Washington, DC 20375, USA.

K. Nielsen, Computational Physics, Inc., 1650 38th St., Suite 105W, Boulder, CO 80301, USA. (knielsen73@gmail.com)